International Ocean Discovery Program Expedition 364 Preliminary Report

Chicxulub: drilling the K-Pg impact crater

In collaboration with the International Continental Scientific Drilling Program

Platform operations
5 April–31 May 2016

Onshore Science Party
21 September–15 October 2016

Sean Gulick, Joanna Morgan, Claire L. Mellett, and the Expedition 364 Scientists

IODP
INTERNATIONAL OCEAN DISCOVERY PROGRAM

Publisher's notes

Core samples and the wider set of data from the science program covered in this report are under moratorium and accessible only to Science Party members until 15 October 2017.

This publication was prepared by the European Consortium for Ocean Research Drilling (ECORD) Science Operator (ESO) and Texas A&M University (TAMU) as an account of work performed under the International Ocean Discovery Program (IODP). Funding for IODP is provided by the following international partners:

National Science Foundation (NSF), United States
Ministry of Education, Culture, Sports, Science and Technology (MEXT), Japan
European Consortium for Ocean Research Drilling (ECORD)
Ministry of Science and Technology (MOST), People's Republic of China
Korea Institute of Geoscience and Mineral Resources (KIGAM)
Australia-New Zealand IODP Consortium (ANZIC)
Ministry of Earth Sciences (MoES), India
Coordination for Improvement of Higher Education Personnel (CAPES), Brazil

Portions of this work may have been published in whole or in part in other IODP documents or publications.

Disclaimer

Any opinions, findings, and conclusions or recommendations expressed in this publication are those of the author(s) and do not necessarily reflect the views of the participating agencies or TAMU.

Copyright

Citation

Gulick, S., Morgan, J., Mellett, C.L., and the Expedition 364 Scientists, 2017. *Expedition 364 Preliminary Report: Chicxulub: Drilling the K-Pg Impact Crater.* International Ocean Discovery Program. http://dx.doi.org/10.14379/iodp.pr.364.2017

ISSN
World Wide Web: 2372-9562

February 2017

Expedition 364 participants

Expedition 364 Science Party

Joanna Morgan*
Co-Chief Scientist/Geophysicist
Department of Earth Science and Engineering
Imperial College London
London SW7 2AZ
United Kingdom
j.morgan@imperial.ac.uk

Sean Gulick*
Co-Chief Scientist/Geophysicist
Institute for Geophysics
Jackson School of Geosciences
University of Texas at Austin
Austin Texas 78758-4445
USA
sean@ig.utexas.edu

Claire Mellett*
Expedition Project Manager
ECORD Science Operator
British Geological Survey
The Lyell Centre
Research Avenue South
Edinburgh EH14 4AP
United Kingdom
cmell@bgs.ac.uk

Johanna Lofi*
Petrophysics Staff Scientist
ECORD Science Operator
Géosciences Montpellier
Université de Montpellier
34095 Montpellier Cedex 05
France
Johanna.Lofi@gm.univ-montp2.fr

Elise Chenot
Inorganic Geochemist
Biogéosciences Laboratory
UMR 6282 CNRS
Université de Bourgogne-Franche Comté
21000 Dijon
France
elise.chenot@u-bourgogne.fr

Gail Christeson*
Geophysicist
Institute for Geophysics
Jackson School of Geosciences
University of Texas at Austin
Austin Texas 78758-4445
USA
gail@ig.utexas.edu

Philippe Claeys
Impact Petrologist
Analytical, Environmental and Geo-Chemistry
Vrije Universiteit Brussel
Pleinlaan 2
1050 Brussels
Belgium
phclaeys@vub.ac.be

Charles Cockell*
Microbiologist
Centre for Astrobiology
School of Physics and Astronomy
University of Edinburgh
Edinburgh EH9 3FD
United Kingdom
c.s.cockell@ed.ac.uk

Marco Coolen*
Organic Geochemist/Microbiologist
Department of Chemistry
Curtin University
Bentley WA 6102
Australia
Marco.coolen@curtin.edu.au

Ludovic Ferrière
Impact Petrologist
Natural History Museum
Burgring 7
1010 Vienna
Austria
ludovic.ferriere@univie.ac.at

Catalina Gebhardt
Physical Properties Specialist
Alfred Wegener Institute Helmholtz Centre of Polar and Marine Research
27568 Bremerhaven
Germany
Catalina.Gebhardt@awi.de

Kazuhisa Goto
Sedimentologist
Tohoku University
International Research Institute of Disaster Science
Aoba 468-1 E303
Sendai 980-0845
Japan
goto@irides.tohoku.ac.jp

Heather Jones
Paleontologist
The Pennsylvania State University
336 Deike Building
University Park PA 16802
USA
hlj123@psu.edu

David Kring
Impact Petrologist
Lunar and Planetary Institute
3600 Bay Area Boulevard
Houston TX 77058
USA
kring@lpi.usra.edu

Christopher Lowery*
Paleontologist
Institute for Geophysics
Jackson School of Geosciences
University of Texas at Austin
Austin Texas 78758-4445
USA
chris.lowery09@gmail.com

Rubén Ocampo-Torres
Organic Geochemist
Groupe de Physico-Chimie de l'Atmosphère
ICPEES
UMR 7515 Université de Strasbourg/CNRS
1 Rue Blessig
67000 Strasbourg
France
ocampo@unistra.fr

Ligia Perez-Cruz*
Geochemist
Instituto de Geofísica
Universidad Nacional Autónoma De México
Coyoacán
Ciudad de México CP 04510
México
perezcruz@geofisica.unam.mx

Annemarie E. Pickersgill
Inorganic Geochemist
School of Geographical & Earth Sciences
University of Glasgow
Gregory Building, Lilybank Gardens
Glasgow G12 8QQ
United Kingdom
a.pickersgill.1@research.gla.ac.uk

Michael Poelchau*
Structural Geologist
University of Freiburg
Geology
Albertstraße 23b
79104 Freiburg
Germany
michael.poelchau@geologie.uni-freiburg.de

Auriol Rae*
Geophysicist/Impact Petrologist
Department of Earth Science and Engineering
Imperial College London
London SW7 2AZ
United Kingdom
a.rae14@imperial.ac.uk

Cornelia Rasmussen
Sedimentologist
University of Utah
Department of Geology and Geophysics
115 South 1460 East (FASB)
Salt Lake City UT 84112
USA
rasmussen.cornelia@gmail.com

Mario Rebolledo-Vieyra
Physical Properties Specialist
Unidad de Ciencias del Agua
Centro de Investigación
Científica de Yucatán, A.C.
77500 Cancún QROO
México
marior@cicy.mx

Ulrich Riller
Structural Geologist
Institut für Geologie
Universität Hamburg
Bundesstrasse 55
20146 Hamburg
Germany
ulrich.riller@uni-hamburg.de

Honami Sato
Inorganic Geochemist
Japan Agency for Marine-Earth Science and Technology
2-15 Natsushima-cho
Yokosuka-city
Kanagawa 237-0061
Japan
honamis@jamstec.go.jp

Jan Smit
Paleontologist
Vrije Universiteit Amsterdam
Faculty of Earth and Life Sciences FALW
de Boelelaan 1085
1018HV Amsterdam
Netherlands
j.smit@vu.nl

Sonia Tikoo
Paleomagnetist
Rutgers University New Brunswick
Earth and Planetary Sciences
Piscataway Township NJ 08854
USA
sonia.tikoo@rutgers.edu

Naotaka Tomioka
Impact Petrologist
Kochi Institute for Core Sample Research
Japan Agency for Marine-Earth Science and Technology
200 Monobe Otsu
Nankoku
Kochi 783-8502
Japan
tomioka@jamstec.go.jp

Michael Whalen
Sedimentologist
University of Alaska Fairbanks
Geosciences
900 Yukon Drive
Fairbanks AK 99775
USA
mtwhalen@alaska.edu

Axel Wittmann*
Inorganic Geochemist
Arizona State University
LeRoy Eyring Center for Solid State Science
Physical Sciences
Tempe AZ 85287-1704
USA
axel.wittmann@asu.edu

Kosei Yamagachi
Inorganic Geochemist
Department of Chemistry
Toho University
Ota-ku Funabashi
Chiba 274-8510
Japan
kosei@chem.sci.toho-u.ac.jp

Long Xiao
Metamorphic Petrologist
China University of Geosciences (Wuhan)
School of Earth Sciences
Planetary Science Institute
388 Lumo Road Hongshan District
China
longxiao@cug.edu.cn

William Zylberman
Paleomagnetist
Aix Marseille University
CNRS IRD Coll France
CEREGE
13626 Aix-en-Provence
France
zylberman@cerege.fr

Additional participants

Jaime Urrutia Fucugauchi
Mexican Scientific Coordinator
Institute of Geophysics
UNAM Board of Governors
National University of México
Coyoacan 04510 México City
México
juf@geofisica.unam.mx

Tim Bralower†
Paleontologist
The Pennsylvania State University
535 Deike Building
University Park PA 16802
USA

ECORD Science Operator (ESO) personnel and technical representatives

David Smith
Offshore Operations Manager

Ursula Röhl
Onshore Operations Manager/ESO Laboratory and Curation Manager

Zeinab Adeyemi
EPC Petrophysics Technician

Susanne Alfken
MARUM Micro-XRF Operator

Vera B. Bender
ESO Data Management Trainee

Laurent Brun
EPC Logging Engineer

Gareth Carter
Expedition Project Manager (EPM)

Carol Cotterill
ESO Outreach Officer

Nataliya Denchik
EPC Petrophysics Technician

Jez Everest
ESO Drilling Coordinator

Annick Fehr
EPC Petrophysics Technician

Thomas Frederichs
ESO Paleomagnetist

Patrizia Geprägs
Assistant Laboratory Manager

Sophie Green
Expedition Project Manager (EPM)

Gilles Henry
EPC Logging Engineer

Grace Howe
EPC Petrophysics Technician

* Participated in shipboard and shore-based operations.

† Participated in shipboard operations only.

Brit Kokisch
LECO Operator

Martin Kölling
MARUM Inorganic Geochemistry Laboratory Manager

Holger Kuhlmann
Core Curator/Assistant Laboratory Manager

Kevin Kurtz
Education Officer

Erwan Le Ber
EPC Petrophysics Staff Scientist

Vera Lukies
ESO Petrophysics Technician

Barbara Matyssek
Education Officer

Garry McGowan
ESO Drilling Coordinator

Mary Mowat
ESO Database Manager

Silvana Pape
MARUM Inorganic Geochemistry Laboratory Technician

Jehanne Paris
EPC Logging Engineer

Laurence Philpott
EPC Petrophysics Technician

Ulrike Prange
ESO Outreach Officer

Connor Richardson
ESO Drilling Coordinator

Luzie Schnieders
ESO Geochemist

Alyssa Stephens
Publications Specialist (JRSO)

Graham Tulloch
ESO Drilling Coordinator

Christoph Vogt
XRD Laboratory Manager

Hans-Joachim Wallrabe-Adams
ESO Data Manager

Jenny Wendt
MARUM Micro-XRF Operator

Thomas Westerhold
ESO Petrophysicist

Alex Wülbers
Core Curator/Logistics

BCR/MARUM, University of Bremen (temporary student assistants)

Roles included core handling, core splitting, sampling, data entry, outreach, and catering

Dennis Flenner

Tugdual Gauchery

Lara Jacobi

Lisa Mehringer

Nina Rohlfs

Jana Schroeder

Jan Unverfährt

Alexander Weise

DOSECC Exploration Services LLC

Christopher Delahunty

Beau Marshall

Skyler Davis

Curt Marrington

Steve Cole

Richard Szentmiklosi

Anthony Vecchiarelli

Will Samuels

Christian Jensen

Michael Vinson

Justin Blouin

Jess Valeda

Vertical seismic profile contractors

Doug Schmitt
VSP Team Leader (University of Alberta)

Randy Kofman
VSP Acquisition (University of Alberta)

Christopher Nixon
VSP Acquisition (University of Alberta)

Steffen Saustrup
VSP Acquisition (University of Texas at Austin)

Weatherford International Ltd. (CT scanning)

Barry Newton

Enthought (CT software developer)

Brendon Hall

Eric Jones

Nora Deram

Liftboat Myrtle—Montco Offshore Inc. (operational staff)

Joe Orgeron
Co-Owner of Montco Offshore Inc.

Burnell Dominique
Captain

Ronald J. Danos
Captain

Roland Marshall
Captain

Tom Overby
Captain

Randy Trosclair
Captain

Cory Caillouet
Mate

Kyle Darda
Mate

Keith Randazzo
Mate

Joe Lindsey
Engineer

Matthew Beavers
Engineer

Chris Saucier
Engineer

Dwayne Duke
Engineer

Keith Krzynowek
Engineer

Mike Krounce
Able Seaman

Jordon Faigot
Able Seaman

Harian Reynolds
Able Seaman

Derek Terrebonne
Able Seaman

Isaias Alamilla
Able Seaman

Robbie Naccio
Able Seaman

Andrew Powell
Ordinary Seaman

Timothy Ellis
Chef

Jimmie Brown
Chef

Elias Trevino
Chef

Michael Brown
Chef

Mexican observer (Mexican Navy)

Socrates Ibarra

Abstract

The Chicxulub impact crater, México, is unique. It is the only known terrestrial impact structure that has been directly linked to a mass extinction event and the only terrestrial impact with a global ejecta layer. Of the three largest impact structures on Earth, Chicxulub is the best preserved. Chicxulub is also the only known terrestrial impact structure with an intact, unequivocal topographic peak ring. Chicxulub's role in the Cretaceous/Paleogene (K-Pg) mass extinction and its exceptional state of preservation make it an important natural laboratory for the study of both large impact crater formation on Earth and other planets and the effects of large impacts on the Earth's environment and ecology. Our understanding of the impact process is far from complete, and despite more than 30 years of intense debate, we are still striving to answer the question as to why this impact was so catastrophic.

During International Ocean Discovery Program (IODP) Expedition 364, Paleogene sediments and lithologies that make up the Chicxulub peak ring were cored to investigate (1) the nature and formational mechanism of peak rings, (2) how rocks are weakened during large impacts, (3) the nature and extent of post-impact hydrothermal circulation, (4) the deep biosphere and habitability of the peak ring, and (5) the recovery of life in a sterile zone. Other key targets included sampling the transition through a rare midlatitude section that might include Eocene and Paleocene hyperthermals and/or the Paleocene/Eocene Thermal Maximum (PETM); the composition and character of the impact breccias, melt rocks, and peak-ring rocks; the sedimentology and stratigraphy of the Paleocene–Eocene Chicxulub impact basin infill; the chronology of the peak-ring rocks; and any observations from the core that may help us constrain the volume of dust and climatically active gases released into the stratosphere by this impact. Petrophysical property measurements on the core and wireline logs acquired during Expedition 364 will be used to calibrate geophysical models, including seismic reflection and potential field data, and the integration of all the data will calibrate impact crater models for crater formation and environmental effects. The proposed drilling directly contributes to IODP Science Plan goals:

Climate and Ocean Change: How resilient is the ocean to chemical perturbations? The Chicxulub impact represents an external forcing event that caused a 75% level mass extinction. The impact basin may also record key hyperthermals within the Paleogene.

Biosphere Frontiers: What are the origin, composition, and global significance of subseafloor communities? What are the limits of life in the subseafloor? How sensitive are ecosystems and biodiversity to environmental change? Impact craters can create habitats for subsurface life, and Chicxulub may provide information on potential habitats for life, including extremophiles, on the early Earth and other planetary bodies. Paleontological and geochemical studies at ground zero will document how large impacts affect ecosystems and effects on biodiversity.

Earth Connections/Earth in Motion: What are the composition, structure and dynamics of Earth's upper mantle? What mechanisms control the occurrence of destructive earthquakes, landslides, and tsunami? Mantle uplift in response to impacts provides insight into dynamics that differ between Earth and other rocky planets. Impacts generate earthquakes, landslides, and tsunami, and scales that generally exceed plate tectonic processes yield insight into effects, the geologic record, and potential hazards.

IODP Expedition 364 was a Mission Specific Platform expedition to obtain subseabed samples and downhole logging measurements from the sedimentary cover sequence and peak ring of the Chicxulub impact crater. A single borehole was drilled into the Chicxulub impact crater on the Yucatán continental shelf, recovering core from 505.7 to 1334.73 m below seafloor with ~99% core recovery and acquiring downhole logs for the entire depth.

Introduction

Peak rings are rings of hills that protrude through the crater floor within large impact basins on terrestrial planets (Figure **F1**), and there is no consensual agreement on either their formational mechanism or the nature of the rocks that comprise them (Grieve et al., 2008). Geophysical data indicate that the peak ring at Chicxulub is formed from rocks that have low velocity and density, and one explanation for this is that they are highly fractured and porous (Morgan et al., 2000, 2011; Gulick et al., 2013). Immediately after impact, the peak ring was submerged under water and located adjacent to a thick pool of hot impact melt. Hence, we would expect intense hydrothermal activity within the peak ring (Ames et al., 2004; Zürcher and Kring, 2004). This activity may have provided a niche for exotic life forms in a way similar to that of hydrothermal vent systems in the oceans. Drilling the peak ring will allow us to determine the origin, lithology, and physical state of the rocks that form it; distinguish between competing models of peak-ring formation; and document hydrothermal systems, microbiology, and post-impact processes and recovery.

Background

The peak ring

The term "peak ring" was first used to describe the often discontinuous, mountainous ring that rises above the floor of large craters on the moon. Peak rings are internal to the main topographic crater rim (Figure **F1**). Since they were first identified on the Moon, peak rings have been observed in large terrestrial craters on all large silicate planetary bodies. Notably, peak rings do not appear to occur on the icy satellites of Jupiter and Saturn, which indicates that crustal rheology plays a role in their formation. The peak ring is a topographic feature; it protrudes through the impact melt and breccia that lines the floor of the crater and stands above the surrounding terrain. As a result, the unequivocal identification of a peak ring in Earth's largest craters is compromised by inevitable erosion and/or tectonism.

Two seismic experiments were conducted in 1996 and 2005 (Figure **F2**) across the Chicxulub impact structure (Morgan et al., 1997; Gulick et al., 2008). Reflection seismic data image impact lithologies and structures to the base of the crust at about 35 km depth (Christeson et al., 2009; Gulick et al., 2013). The impact basin is buried beneath a few hundred meters of Cenozoic sediments, and the present-day Cretaceous-Paleogene (K-Pg) surface deepens to ~1 s two-way traveltime (~1 km), revealing a ~145 km diameter post-impact basin (Morgan and Warner, 1999) with ring-shaped faults reaching diameters >200 km (Gulick et al., 2008). Within this post-impact basin, there is an ~80 km diameter topographic ring that appears analogous to peak rings observed on other planetary bodies (compare Figures **F1**, **F3**, **F4**). Reflective pre-impact stratigraphy (the Mesozoic sediments) can be tracked around the crater (Whalen et al., 2013), and large offsets in the stratigraphy define a 20–35 km wide terrace (or megablock) zone (Figure **F3**) (Gulick et al., 2008, 2013). Morgan and Warner (1999) argue that the head scarp of this terrace zone is analogous to the crater rim in peak-ring craters (Fig-

ure F1), and rings outside the head scarp (Figure F3) suggest that Chicxulub is a multi-ring basin (Morgan et al., 1997; Gulick et al., 2008). The acquired seismic data show that the water depth was deeper and the Mesozoic sediments thicker in the northeast quadrant of the crater (Bell et al., 2004; Gulick et al., 2008) and that lateral variation in the target at the impact site might explain the current crater asymmetry (Collins et al., 2008). Velocities and densities of the rocks that form the peak ring are low (Morgan et al., 2000; Vermeesch and Morgan, 2008; Barton et al., 2010), and a high-resolution velocity model obtained using full-waveform inversion (Figure F4) shows that the uppermost peak ring is formed from about 100–150 m of rocks with very low *P*-wave velocity (Morgan et al., 2011).

Given the lack of intact peak rings exposed at the Earth's surface, there is no consensus as to either their geologic nature (of what material are they composed and from what stratigraphic location does this material originate) or the mode of formation of a peak ring. Numerical simulations of large-crater formation suggest that they are formed during the collapse of a deep bowl-shaped "transient cavity" formed during the initial stages of cratering (Figure F5A) (Morgan et al., 2000; Collins et al., 2002; Ivanov, 2005; Senft and Stewart, 2009). During this collapse, structural uplift of the crater floor produces a central uplift, which is overheightened and unstable under gravity (Figure F5B). The subsequent outward collapse of the central uplift in some way leads to the formation of a ring of peaks between the crater center and the crater rim (Morgan et al., 2000, 2011). This model for peak-ring formation is consistent with seismic data that show downthrown Mesozoic rocks lie directly beneath the peak ring at Chicxulub at all azimuths (Morgan et al., 2000; Gulick et al., 2013). However, the precise kinematics and details of the mechanics of cavity modification remain unclear. Moreover, that such emphatic collapse of the transient crater occurs at all requires substantial weakening of target rocks relative to their static laboratory-measured strength (Melosh, 1979; O'Keefe and Ahrens, 1993). In numerical models, the precise kinematics of crater collapse and peak-ring formation is dependent on near-surface rheology, as well as the spatial extent, nature, and timing of the weakening of the target rocks (e.g., Wünnemann et al., 2005).

Previous drilling

Petróleos Mexicanos (Pemex) drilled several deep (~1.6 km) holes into or close to the Chicxulub crater (Figure F2), completing their drilling in the mid-1970s (Figure F6A). Unfortunately, the amount of coring was limited, and their interest in the area waned after they intercepted Paleozoic basement and impactites without any sign of hydrocarbons. Very few samples of the impact lithologies found in these wells are now available for examination. The Universidad Nacional Autónoma de México (UNAM) conducted a shallow drilling program in the 1990s, during which impact lithologies were penetrated at three sites: U5, U6, and U7 (Urrutia-Fucugauchi et al., 1996). International Continental Scientific Drilling Project (ICDP) Borehole Yaxcopoil-1 (Yax-1) was drilled ~60 km south-southwest of the crater center (Stöffler et al., 2004; Urrutia-Fucugauchi et al., 2004) within the impact basin and inside a ring of cenotes (Figure F6A). The general stratigraphy of the Chicxulub crater has been constructed using the available core from these programs and the original Pemex logs (Figure F6B, F6C) (Ward et al., 1995; Rebolledo-Vieyra and Urrutia-Fucugauchi, 2004).

The onshore wells indicate that post-impact sediments deepen from a few hundred meters at radii >90 to ~1.1 km within the center of the post-impact basin (Figure F6B); this thickening of the Cenozoic sequence is in agreement with the offshore seismic data. Within the impact basin, Wells C1, S1, and Y6 penetrated a few hundred meters of suevite and 200–500 m of impact melt rock, whereas outside the basin, Wells T1, Y2, Y5A, Y1, and Y4 penetrated a few hundred meters of melt-poor lithic breccia (Hildebrand et al., 1991; Sharpton et al., 1996; Urrutia-Fucugauchi et al., 2011). Several wells penetrated thick sequences of Cretaceous rocks. Close to the structure, these sequences are ~2 km thick and comprise dolomites and carbonates, with some thick beds of Lower Cretaceous anhydrite. Wells Y1 and Y2 penetrated Paleozoic basement at ~3.3 km depth. UNAM Well U5 shows Cenozoic rocks above suevite, and in Well U7, suevitic breccia overlies melt-poor lithic breccia, composed mainly of sedimentary clasts rich in evaporitic material (Urrutia-Fucugauchi et al., 2008). The upper breccias have high magnetic susceptibilities, low seismic velocities, low density, and high porosities and permeabilities; in contrast, the lower breccias show low susceptibilities, variable seismic velocities, and lower porosities and permeabilities (Urrutia–Fucugauchi et al., 1996; Rebolledo-Vieyra and Urrutia-Fucugauchi, 2006). In Well U6, Cenozoic rocks directly overlie this melt-poor lithic breccia, with an erosional contact between them (Figure F6C). The melt-poor lithic breccia in the two UNAM wells could be the same impact breccia observed in Wells Y4, Y1, Y5A, Y2, and T1. No onshore wells have penetrated the peak ring, and no previous offshore wells were drilled into the Chicxulub impact structure.

ICDP Borehole Yax-1 is located ~60 km radial distance from the crater center and is positioned interior of the crater rim. Drilling recovered core from the ~800 m thick Cenozoic sequence, impact breccias, and underlying parautochthonous Cretaceous rocks to 1511 m below the surface (Urrutia-Fucugauchi et al., 2004). The earliest Cenozoic sediments indicate gravity flows and resurge deposits formed part of the initial crater fill (Goto et al., 2004; Whalen et al., 2008, 2013) and contain geochemical evidence for long-lasting hydrothermal venting into the ocean (Rowe et al., 2004; Zurcher and Kring, 2004). Unfortunately, its location on a steep slope meant studies of the post-impact section were plagued by coarse-grained redeposited carbonates and lithification, and the very basal Paleocene appears to be missing (Arz et al., 2004; Smit et al., 2004; Rebolledo-Vieyra and Urrutia-Fucugauchi, 2004; Whalen et al., 2013). The 100 m thick melt-rich impactite sequence is complex and composed of six distinct units (Claeys et al., 2003; Kring et al., 2004; Stöffler et al., 2004; Wittmann et al., 2007), which were modified by post-impact hydrothermal circulation (Hecht et al., 2004). The Cretaceous rocks appear to be formed from a number of megablocks, composed of dolomite, limestone, and about 27% anhydrite, which have rotated relative to each other, probably during the crater modification stage (Kenkmann et al., 2004). The megablock lithologies are intruded by suevitic dikes, impact melt dikes, and clastic, polymict dikes (Wittmann et al., 2004).

Scientific objectives

Expedition 364 was designed to address the following objectives through drilling at Site M0077:

- The nature and formation of a topographic peak ring;
- How rocks are weakened during large impacts to allow them to collapse and form relatively wide, flat craters;
- The nature and extent of post-impact hydrothermal circulation;
- The habitability of the peak ring and effect of this impact on the modern and ancient deep biosphere;

- The recovery of life in a sterile zone;
- The nature of the Eocene and Paleocene hyperthermals and the Paleocene/Eocene Thermal Maximum (PETM) transition;
- The nature and composition of the impact breccias, melt rocks, and peak-ring rocks;
- The volume of dust and climatically active gases released into the stratosphere by this impact;
- The climatic effects of this impact;
- The sedimentology and stratigraphy of the Paleocene–Eocene Chicxulub impact basin infill;
- The chronology of the peak-ring rocks and impact lithologies;
- Petrophysical properties measured on cores and downhole to calibrate geophysical models and integrate with seismic velocity data; and
- Integration of all data to calibrate impact crater models for crater formation and environmental effects.

The nature and formation of peak rings

Hole M0077A sampled material that forms a topographic peak ring (Figure **F4**) and reveals the lithologic and physical state of these rocks, including porosity, fracturing, and extent of shock effects. The recovered core will be used to test the working hypotheses that peak rings are formed from (1) overturned and uplifted basement rocks, (2) megabreccias, or (3) some other material. If the peak ring is formed from uplifted rocks, as predicted by several independent numerical simulations of crater formation (Figure **F5**) (Collins et al., 2002; Ivanov, 2005; Senft and Stewart, 2009), then we can estimate their depth of origin (upper crust or deeper) using metamorphic grade, thermochronology, and possibly remanent magnetism. The orientation of impact-induced discontinuities, which may include breccia zones, brittle shear faults, and melt-filled fractures, will be used to infer the strain geometry (i.e., the orientation) and potentially also the magnitude of the three principal strain axes during peak-ring formation and thus constrain the kinematics of peak-ring formation. Collectively, these data will be used to discriminate between models of peak-ring formation and to groundtruth dynamic models of crater formation (Figure **F5**), which now include dilatancy: the increase in porosity induced during cratering and the cause of the gravity low across impact craters (Collins, 2014). For example, in the numerical simulations shown in Figure **F5**, shock pressures experienced by peak-ring rocks are predicted to be between 10 and 50 GPa, whereas they are expected to be relatively lower on average in the model by Baker et al. (2016), which is based on analyses of peak ring craters on the Moon and Mercury.

The weakening mechanism

Numerical modeling of large impacts indicates that rocks must behave in a fluid-like manner for a short period of time after impact to allow the dramatic collapse of a large bowl-shaped transient cavity to form a broad, flat final crater (Melosh and Ivanov, 1999). In these models, the material that forms the peak ring has traveled the greatest distance during crater formation (e.g., Figure **F5**) and thus should have undergone the most mechanical weakening. Providing a physical explanation for the apparent transitory low strength of the target is an enduring and challenging problem in impact cratering mechanics. Proposed weakening mechanisms include acoustic fluidization (Melosh, 1979; Melosh and Ivanov, 1999), thermal softening (O'Keefe and Ahrens, 1993), and strain-rate weakening (Senft and Stewart, 2009). Geological investigations at complex craters provide clues to the weakening mechanism, such as evidence for cataclastic flow (Kenkmann, 2003) and the identification of individual blocks surrounded by breccias in accordance with the block model of acoustic fluidization (Ivanov, 1994; Kenkmann et al., 2005; Riller and Lieger, 2008). Eroded complex craters often possess large zones of pseudotachylytic breccia, which may act to reduce friction on fault planes (Spray, 1992; Reimold and Gibson, 2005; Mohr-Westheide et al., 2009; Riller et al., 2010), although this appears to conflict with observational data that suggests melt was emplaced in a tensional stress regime (Lieger et al., 2009).

Quasistatic mechanical loading tests of intact and brecciated target material will be used to measure the strength difference between friction-controlled deformation of crushed rock and fracture-controlled deformation of intact rock. Such data, along with our analyses of samples of the peak-ring rocks, will be used to investigate what mechanism(s) allow the target rocks to behave temporarily as a fluid in response to hypervelocity impact.

Hydrothermal circulation

Both the post-impact sediments and peak-ring rocks will be examined for evidence of hydrothermal alteration and post-impact venting into the ocean to answer questions such as how long did the circulation last, and how high was the maximum temperature? Models of hydrothermal systems in impact craters imply enhanced flow in peak rings (e.g., Figure **F7**) (Ames et al., 2004; Zürcher and Kring, 2004; Schwenzer and Kring, 2009), and thus Site M0077 is an excellent location to investigate the hydrothermal system at Chicxulub. This line of inquiry will include petrological assessment and thermochronology, as well as X-ray diffraction (XRD), X-ray fluorescence (XRF), fluid inclusion, and stable isotope analyses to examine the alteration assemblage and characterize the composition of the hydrothermal fluids (Ames et al., 2004; Lüders and Rickers, 2004; Zürcher and Kring, 2004; Osinski et al., 2005, 2013). Was hydrothermal circulation focused in specific zones, as it was in Hole Yax-1 (along faults and lithologic contacts), or was it more pervasive? Wireline logs and petrophysical measurements on the core will be used to measure fracture density and porosity, which will help assess ancient permeability—an important parameter in modeling hydrothermal systems (Abramov and Kring, 2007).

Deep biosphere and habitability

Analyses at different depths of the borehole focusing on samples of melt, crystal xenoliths embedded in the melt, and crystals from the peak ring itself will be used to determine the duration of the crater cooling from 500°C to below 200°C and ultimately provide better quantification on how long a crater stays warm enough to be suitable for life evolution and deep subsurface microbial communities.

Both the post-impact sediments and peak-ring rocks will be examined for present-day microbiology and biosignatures of past life. Impacts can have an adverse effect on the deep biosphere due to hydrothermal sterilization, but they may also lead to an increase in microbial abundance due to impact-induced fracturing (Cockell et al., 2002, 2005). The diversity of microbial life will be quantified and compared with geological and geochemical data to answer questions such as was the microbiology shaped by the post-impact hydrothermal system, and did organic matter get trapped within hydrothermal minerals? The deep biosphere will be investigated using culturing, molecular biological analyses of DNA, searching for biosignatures such as hopanoids and other lipids/biomolecules, and paired analyses of paleome (the genome of an extinct species) and lipid biomarkers (Cockell et al., 2005; 2009; Coolen and Overmann, 2007; Coolen et al., 2013). Iron isotopes will also be used to detect biosignatures because they are particularly useful for studies of an-

cient, severely metamorphosed and/or altered rocks (Yamaguchi et al., 2005). The rehabitation of the deep biosphere following a large impact, as seen at the Chesapeake impact structure (Figure **F8**), will shed light on whether peak rings and impact breccias are an ecological niche for exotic life and thus potentially important habitats for early life on Earth (Kring and Cohen, 2002; Bryce et al., 2015).

Recovery of life

Immediately after impact, the ocean was likely sterile, at least locally. We will use core through the post-impact sediments to examine the recolonization of the ocean, including what biota came back first (benthic versus planktonic, dinoflagellates, specialists versus generalists), how long it took to return to normal conditions, and whether cold-water species returned quickly. Of interest will be nannoplankton recovery at "ground zero" in comparison to the global response (e.g., Jiang et al., 2010). There was likely a significant lag in recovery due to a long-term, impact-initiated hydrothermal circulation system (Abramov and Kring, 2007). Did diversity gradually recover with the hardiest taxa appearing first and other taxa taking longer to populate the impact basin, or did the whole assemblage return simultaneously once the environment stabilized? Reconstruction of the environment of the earliest Paleocene will be achieved using stable carbon and oxygen isotopes of planktonic and benthic foraminifers and fine-fraction carbonates, as well as stable carbon and nitrogen isotopes of sedimentary organic matter. These analyses combined with major and trace element proxies for biologic productivity and redox conditions will inform the paleoceanographic conditions in the basin after impact and provide clues to when normal marine carbon and nitrogen cycling were restored. Study of biomarkers at the molecular level (high-pressure liquid chromatography [HPLC] and liquid chromatography–mass spectrometry [LC-MS]) and pigments (chlorophylls, bacteriochlorophylls, and its degradations products) from photosynthetic organisms (algae and photosynthetic bacteria) may indicate changes in and evolution of photosynthetic organism populations after impact.

It is expected that both marine and terrestrial organic matter have accumulated in the post-impact sediments and that the paired stratigraphic analysis of the paleome and lipid biomarkers and their isotopic compositions using precisely dated core material will provide detailed insights into post-impact environmental conditions and the recovery and evolution of surface and deep subsurface life (Coolen et al., 2007, 2013). Of interest is the ocean chemistry and temperature immediately following the impact and any indicators of climatic recovery. Are there signs of local hydrothermal venting (Zürcher and Kring, 2004), short-term global cooling (Vellekoop et al., 2014), and/or indicators of ocean acidification? How long did it take to return to normal conditions? Oxygen isotope ratios, in particular, may help constrain surface and bottom water temperatures in the immediate post-impact interval. Intrinsic magnetic properties of sediments can be used as proxy of the relative abundance of biogenic versus detrital fraction in the sediments, and changes in magnetic mineralogy can be attributed to changes in the depositional environment (redox conditions, detrital source, etc.).

Eocene and Paleocene hyperthermals and the PETM transition

Transient warm events during the "greenhouse" phase of Earth's climate history, also called hyperthermals, are key insights into the feedbacks in the climate system. The Paleocene to Eocene intervals cored during Expedition 364 are particularly interesting due to the potential to recover the PETM, as well as late Paleocene and early Eocene events (Figure **F9**). Sedimentary records of many PETM transitions and hyperthermals suffer from poor preservation due to dissolution. The section we recovered at Chicxulub is atypical, as it is in a subtropical location and within a semi-isolated basin above the calcium compensation depth (CCD); therefore, carbonate sediment accumulation should have been maintained throughout the Paleocene and Eocene.

Key to understanding any recovered hyperthermal intervals including the PETM will be the documentation of changing paleoceanographic conditions (depth and redox state), sedimentary environments, and biological productivity. Biological productivity will be evaluated through analysis of total organic carbon, stable isotopes from organic matter (C, N) and carbonates (C, O), and XRF geochemical analyses to determine concentrations of micronutrients such as Cu, Ni, and Zn. XRF analyses of redox-sensitive trace metals (Cr, Ni, Mo, V, and Ur) will provide insight into bottom water oxygenation during the PETM and Eocene hyperthermals. Biomarkers may distinguish between terrestrial and methane hydrates and thus help constrain the cause of warming. High-resolution biostratigraphy and magnetostratigraphy will be used to obtain a robust age model in the post-impact sediments and identify key events in the cored interval, including the hyperthermals and PETM.

Changes in continental weathering during the Paleocene–Eocene transition will be evaluated through studying clay mineralogy. There was an intensified hydrological cycle and warming across the PETM (Zachos et al., 2001), and inputs of kaolinite, illite, palygorskite, and/or sepiolite into sedimentary basins during this period have been linked to an increase in runoff (John et al., 2012).

Impact breccias, melt rocks, and peak-ring rocks

Chicxulub breccias appear to be quite variable, in particular with respect to the amount of anhydrite and the lithology and age of basement clasts (Kettrup et al., 2000; Kring, 2005; Urrutia-Fucugauchi et al., 2008). The mineralogical and geochemical characterization of the impactites and peak-ring rocks will provide key information on target rock composition (Koeberl et al., 2012). We will also search for an extraterrestrial signature using platinum group element (PGE) analyses and Os and Cr isotopes (Gelinas et al., 2004; Tagle and Hecht, 2006; Trinquier et al., 2006; Goderis et al., 2012; Sato et al., 2013, 2015) to determine whether a measurable fraction of the projectile remains at the impact site or whether most projectile material ends up within the global K-Pg layer (Artemieva and Morgan, 2009). High-resolution $^{40}Ar/^{39}Ar$ analyses and electron microscopy on shocked and melted impactites, as well as U/Pb dating of zircon and other thermochronometers, will be used to study their pressure-temperature-time and deformational history and for high-precision dating of the Chicxulub impact. Shock metamorphism of the feldspathic components will be used to investigate how impact processes affect argon (Ar) retention (Pickersgill et al., 2015). Shock metamorphism and pyrometamorphic indicators for rock-forming minerals will help constrain peak shock pressure and temperature regimes (Grieve et al., 1996; Tomioka et al., 2007; Wittmann et al., 2009; Huber et al., 2011; Rae et al., 2015). Compositional and structural investigations of any intruded dikes will allow assessment of their origin, energy of emplacement, and timing and, for example, discover whether melt within dikes is more mafic than the impact melt in the central crater, as it is in Borehole Yax-1 (Wittmann et al., 2004).

Magnetic susceptibility and paleomagnetic measurements will be used to investigate whether hydrothermal circulation led to the formation of ferromagnetic minerals and a chemical remanent magnetization (Quesnel et al., 2013). These measurements will also us to evaluate whether hydrothermal circulation is the source of the strong magnetic anomaly recorded at surface and whether a component of the natural remanent magnetization (NRM) is shock induced (Tikoo et al., 2015) or is detrital remanent magnetization, as it is in the post-impact sediments in Borehole Yax-1 (Rebolledo-Vieyra and Urrutia-Fucugauchi, 2004).

Dust, climatically active gases, and wildfires

The study of the shock and thermal effects recorded in the carbonate and evaporite impactites will help to constrain more precisely the degassing process of carbonates and evaporates from the Yucatán target rock. Placing constraints on the impact energy with numerical simulations and on the lithology, shock state, and porosity of the target rocks is important because these are all critical input parameters for modeling the environmental effects of this impact (Pope et al., 1997; Pierazzo et al., 2003). Solid, melted, and vaporized material from the asteroid and target rocks are ejected away from the impact site within an expanding plume (Figure **F10**), and the mass, velocity, and composition of these ejecta are dependent on impact angle (Artemieva and Morgan, 2009; Morgan et al., 2013). The duration and strength of the thermal pulse delivered at the Earth's surface by reentering ejecta varies with direction and distance from Chicxulub (Morgan et al., 2013), and this variation affects the likelihood of ignition of flora (Belcher et al., 2015). Geophysical and drill core data and 3-D numerical simulations of the impact will be used to constrain impact angle and direction and better constrain the intensity of the thermal pulse around the globe.

Post-impact sequence, including resurge and/or tsunami deposits

Was the peak ring (being a topographic high) protected from resurge deposits? Or is it covered by wash-back deposits such as multitiered, coarse-grained, reworked impact breccias or cross-bedded sediments overlain by a K-Pg Ir-rich layer? What is the history of peak-ring burial within the impact basin into the Eocene?

We will investigate the uppermost peak-ring deposits to determine the events immediately post-impact. There may be evidence of repeated tsunami and seiche surges, as observed at Brazos River, Texas (USA), in the form of several distinct graded layers (Vellekoop et al., 2014).

We will also use drilling, a vertical seismic profile (VSP) experiment, and other logging data to identify the borehole depths and core-based lithologic contrasts that generate horizons in our reflection data (Figures **F2**, **F3**, **F4**). With this core-log-seismic mapping, we can identify the stratigraphic age of reflectors and map these across the impact basin using the extensive suite of seismic reflection data acquired in 1996 and 2005. Sedimentological and stratigraphic data are key to understanding the paleoceanographic and sea level history across this impact basin (Whalen et al., 2013). Detailed biostratigraphic and sedimentologic studies including analysis of grain size, mineralogy, sedimentary structures, and ichnofabric using the cores and X-ray computed tomography (CT) scans will be crucial in documenting the post-impact sedimentary history. Radioisotopic dating of ash layers in the post-impact section will be used along with magnetostratigraphic and biostratigraphic analyses to investigate the volcanic history of this portion of the Gulf of Mexico and to additionally constrain the post-impact age model. Drill core data will be used to groundtruth seismic reflectors, which can be tracked into adjacent deep-water sections to help understand the nature of lower Cenozoic sequences in the Gulf of Mexico, which are difficult to date due to the lack of publicly available scientific cores. This mapping into the broader Gulf of Mexico will enable testing of models for large-scale basin margin collapse caused by impact generated earthquakes and tsunami (Sanford et al., 2016).

Chronology of peak-ring rocks and impact lithologies

Of key interest is the age of the Chicxulub impact and the resulting K-Pg boundary deposits that it caused (Renne et al., 2013; Schulte et al., 2010). Therefore, a goal of the expedition was to determine the ages of impact lithologies and impact melt and any reset ages on uplifted target rocks at the impact site. This work will be accomplished through Ar/Ar and U/Pb ages on impact glasses and Ar/Ar dating of feldspars paired with U/Pb dating of zircons. Additionally, a range of thermochronometers will be explored within the drilled samples to investigate pressure-temperature-time paths within the peak ring.

Petrophysical groundtruth and geophysical integration

Wireline logging and petrophysical measurements on the core will be used to groundtruth potential fields' geophysical models (gravity, magnetic, refraction, and magnetotelluric data) and integrate with 2-D and 3-D seismic velocity data. Core- and borehole-based measurements will be critical to improving our understanding of crater structure away from the drill hole, in particular onshore where deep borehole and seismic data are sparse to nonexistent. Drilling will allow us to address questions such as what is the cause of the strong magnetic anomaly recorded at surface, and what is the cause of the low seismic velocities and densities within the peak ring (are these fractured deep-crustal basement rocks, megabreccia, or some other material), and is the thin (100–150 m thick) layer of very low velocity rocks forming the uppermost lithology of the peak ring composed of impact breccias? We will also use borehole imaging to constrain dips within the peak ring stratigraphy to test for overturning during emplacement and verify whether the dips are consistent with the observed inward-dipping reflectors and region of lowered velocities. Magnetic properties of the impactites and peak-ring rocks can be used to investigate causes of the magnetic anomaly data throughout the crater and as a tool to correlate between onshore boreholes and offshore Site M0077.

Operational strategy

Expedition 364 was drilled using a Mission Specific Platform due to the relatively deep target depth (1500 m drilling depth below seafloor [DSF]) and shallow-water location (19.8 m). In order to meet the scientific aims, an Atlas Copco T3WDH mining rig was cantilevered from the bow of the jack-up platform, the *L/B Myrtle*. The vessel was contracted from Montco Offshore with drilling services provided by Drilling Observation and Sampling of the Earths Continental Crust (DOSECC).

The downhole logging program was managed by the European Petrophysics Consortium (EPC), and the University of Alberta

(Canada) and the University of Texas at Austin (USA) were contracted to carry out the VSP measurements.

The first phase of mobilization began on 12 March 2016 in Fourchon, Louisiana (USA). The vessel transited to the drill site (with refueling and weather delays), arriving on station on 5 April. The final mobilization was completed on station, and the offshore operational phase began with open-hole drilling on 8 April. Operations continued for 48 days, culminating on 26 May. Following a final phase of downhole logging, the vessel returned to Progreso, Mexico, before continuing transit back to Fourchon for full demobilization.

A single hole was drilled. A series of drill strings of reducing diameters were utilized in order to maximize the likelihood of reaching the target depth. The borehole configuration comprises the following components (Figure **F11**):

- Open-hole drilling:
  - 12¼ inch open-hole drilling from the seabed to 15.5 m DSF
  - 9⅝ inch casing and cementation to 15.5 m DSF
  - 7⅞ inch open-hole drilling from 15.5 m to 503.6 m DSF
  - 6⅝ inch casing and cementing to 503.6 m
  - The base of the hole was advanced to 505.7 m DSF whilst clearing cement and debris from the bottom of the hole
- Coring:
  - Coring with oversize PQ3, (outer diameter [OD] 5.875 inches [149.225 mm]) from 505.7 to 707.1 m DSF, producing an ~83 mm diameter core.
  - 5½ inch casing was set to 701 m DSF before changing the core barrel and bit size.
  - Coring with PQ3, (OD 4.827 inches [122.6058 mm]) From 707.1 m DSF to the base of the hole at 1334.69 m DSF, maintaining ~83 mm diameter cores.

Table **T1** summarizes hole details and recovery.

The downhole logging strategy involved a similar stepwise approach to ensure logs were collected from the maximum interval possible. Details of the downhole logging program are summarized in **Downhole logging**.

During the operational phase of Expedition 364 from 5 April to 30 May 2016, 2.67% of the operations time was spent mobilizing, 0.22% in transit, and 11.48% on downtime due to equipment. The remaining 85.67% of the offshore phase was for drilling, coring, and downhole logging operations.

Principal results

Open-hole drilling occurred from the seabed to ~500 m DSF, and core was recovered between 505.70 and 1334.73 meters below seafloor (mbsf). Attempts to recover drilling cuttings from the open-hole section were largely unsuccessful due to loss of the drilling fluid into the formation. In the upper cores, a sequence of post-impact sediments was recovered between 505.70 and 617.28 mbsf. The peak-ring rocks recovered comprise suevite above clast-poor impact melt rock from 617.28 to 747.14 mbsf. This interval overlies shocked felsic basement rocks intruded by pre-impact mafic and felsic igneous dikes as well as suevite and impact melt rock between 747.14 and 1334.73 mbsf.

Results are divided into four sections that reflect the key lithological and structural sequences encountered in Hole M0077A:

- Open hole: 0–505.7 m DSF
- Post-impact sediments: Core 1R to Section 40R-1, 109.4 cm (505.70–617.28 mbsf)
- Upper peak ring (suevite and impact melt rock): Section 40R-1, 109.4 cm, to base of Core 95R (617.28–747.14 mbsf)
- Lower peak ring (granitoids, pre-impact dikes, suevite, and impact melt rock): Cores 96R through 303R (747.14–1334.73 mbsf)

The divisions chosen here are based on observations of core and logging data only. These intervals do not represent the precise locations of lithologic boundaries within the core.

Lithostratigraphy and CT facies

Lithostratigraphy

Post-impact sediments

The post-impact sedimentary rocks of Hole M0077A consist of a diverse suite of lithologies including claystone, black shale, dark marlstone/claystone, marlstone, siltstone, and limestone divided into wackestone, packstone, and grainstone. Most lithologies are dominantly fine grained (clay to silt sized) except for local grainstones that contain clasts that are dominantly sand sized. Most lithologies have examples of planar to wavy laminated textures with ichnofabric indexes of 1 to 2 or are bedded at the centimeter scale. Thicker bedded units are dominantly bioturbated with ichnofabric indices of 3 to 5. Cyclic or rhythmic arrangement of lithologies is common, with cycles typically grading upward from dark marlstone/claystone through marlstone and wackestone and/or packstone. Except locally (i.e., Core 37R-1), grainstones are thin, laminated, or cross-laminated packages intercalated with finer grained facies.

The relative distribution and proportions of different lithologies, as well as specific surfaces indicating erosional truncation of underlying facies or abrupt change in lithology, were used to divide the post-impact sedimentary rocks into different lithostratigraphic subunits (1A–1G; Table **T2**). Most subunits are between 20 and 27 m thick except for Subunits 1B, 1F, and 1G, which are all less than 10 m thick. Subunit 1A is dominated by dark marlstone/claystone. Unit 1B is mainly limestone with intercalated marlstone and dark marlstone/claystone. Subunits 1C and 1D are largely composed of dark marlstone/claystone but also contain marlstone and limestone. Subunits 1E and 1F are primarily wackestone and packstone. Subunits 1D and 1E are the only units that contain black shale. All units have sporadic rare to common beds of bluish claystone that were likely deposited as volcanic ash. Subunit 1G is very thin (<1 m) and unusual lithologically as a fining-upward calcareous siltstone dominated by thin rhythmic alternations of darker and lighter colored laminae or beds that form the base of the post-impact sedimentary succession. The inclusion of greenish clasts of glass in the lower part of the unit signals the transition to the underlying suevite of Subunit 2A (Table **T2**).

Peak ring

From Section 40R-1, 109.4 cm, to the end of the drill cores at Section 303R-3, 56 cm, a succession of Chicxulub crater impactites occur, comprising suevites, impact melt rocks, and shocked basement rocks.

The upper peak ring consists of an impactite sequence from Section 40R-1, 109.4 cm, to Section 87R-2, 90 cm, and is divided into two units: Units 2 and 3 (Table **T2**). Unit 2 contains 104 m of suevites with impact melt rock clasts, as well as lithic clasts from the carbonate platform and basement ranging in size from submillimeter to over 25 cm. Clasts are subangular to subrounded. The suevite

matrix is a fine-grained, micritic carbonate. Subunit 2A is characterized by repeated fining-upward or coarsening features in the suevites with clast sizes <2 cm. The transition to Subunit 2B in Section 55R-3, 11 cm, is the lowest erosional contact observed in Unit 2. Subunit 2B consists of a single 48 m fining-upward succession. Subunit 2C begins at Section 83R-1, 75 cm, with a gradational change to a ~9 m thick, dark brown suevite matrix with very poorly sorted angular to subangular clasts.

Unit 3 begins at Section 87R-2, 90 cm, and is composed of impact melt rock with abundant (>25%) clasts. It is divided into two subunits. Subunit 3A is characterized by a 16 m thick mixture of green and black melt. The green material sometimes forms a matrix with angular fragments of black melt and can be intimately intermixed with black melt, forming schlieren of green material. Within the black melt are found centimeter- to decimeter-sized clasts of target material composed of metamorphic and igneous target lithologies, including decimeter-sized clasts of granodiorite and gneiss. Subunit 3B is ~9.5 m thick coherent black melt unit that begins at Section 92R-3, 17 cm. Clasts are composed of metamorphic and igneous target lithologies, but the subunit lacks visible clasts of sedimentary lithologies. Clasts of granite dominate and increase in abundance toward the base of the subunit and are up to 42 cm in diameter.

Beneath Section 95R-3, 117 cm, the lower peak ring recovered at Site M0077 includes a long succession of felsic basement rocks of granitoid composition (Unit 4). Petrographically, these rocks are characterized chiefly by coarse-grained granite to syenite hosting aplite and pegmatite dikes. Moreover, granitoid rocks are intruded by three types of subvolcanic dikes or dike swarms including felsite, dacite, and diabase/dolerite. Petrographic analysis shows that this suite of basement rocks is pervasively shocked, with quartz and feldspar grains displaying planar deformation features throughout the entire unit. Granitoids also show localized zones of pervasive shearing and deformation, with notable millimeter to centimeter thick cataclastic bands and microbrittle foliation.

Granitoid basement rocks host several smaller bodies of suevite and impact melt rock (15 cm to 4 m thick). An approximately 100 m thick unit of suevite and impact melt rock occurs at 1215–1316 mbsf (Cores 265R–298R). These two lithologies form a nearly continuous unit, with only a few decimeter- to meter-scale intercalations of granite. Flow banding occurs in both the impact melt rock and suevite. Clasts are melt fragments, granite, and other basement lithologies and are characterized by a notable lack of carbonates compared to the suevites and impact melt rocks in the upper peak ring. Granitic rocks were cored in Cores 298R–303R, and the final Sections 303R-2 and 303R-3 of the borehole consist of a 78 cm thick polymict breccia mingled with impact melt rock.

CT facies

CT facies were described throughout the hole. Distinctions between different CT facies were made on the basis of CT values, bulk density (ρ_b), effective atomic number (Z_{eff}), and common textures. In general, CT facies show a good match with the lithologic boundaries and lithostratigraphic units identified during visual core description. CT facies are described in the context of higher and lower CT values. Similar lithologies usually display similar CT values and are represented by a grayscale color scheme. In addition, CT values are compared to images of ρ_b and Z_{eff}.

Post-impact sediments

CT scans of individual lithologies and the defined units of post-impact sediments were described. Marlstone and dark claystone/marlstone lithologies can be associated with light gray and dark gray intervals that display mainly low ρ_b and high Z_{eff} values. Overall, the reoccurring, relatively thin claystone layers are represented by black CT intervals that correspond to relatively low ρ_b and Z_{eff} values. The wackestones and packstones of the limestone lithologies are mainly associated with light to dark gray and black intervals that reflect a broad spectrum of ρ_b and Z_{eff} values. The grainstone lithology presents itself uniformly as a light gray interval associated with high ρ_b and Z_{eff} values.

A CT facies is also defined for the lithostratigraphic units (Subunits 1A–1G). Subunits 1A–1C show light gray, dark gray, and black intervals that are associated with low ρ_b and high Z_{eff}, values (Subunits 1A and 1C) and relatively high ρ_b and Z_{eff}, values (Subunit 1B). Subunit 1D is still represented by the same color scheme, but the black and white intervals increase in thickness. The ρ_b and Z_{eff}, values vary depending on the represented lithology (e.g., interbedded marlstones). Subunits 1E and 1F consist predominantly of one light gray CT interval with a few thin dark gray to black areas. The light gray can be correlated with high but also low Z_{eff} and quite variable density values. Subunit 1G is represented by light to dark gray intervals that are overall associated with relatively high ρ_b and high Z_{eff}.

Upper peak ring

CT facies for Units 2 and 3 were described during visual core description. The subunits of Units 2 and 3, divided by visual core description alone, can be clearly seen in the CT data. Additionally, certain subunits (e.g., Subunit 2C) have abrupt and unusual changes in CT character throughout the unit.

Unit 2 has an overall trend of increasing CT number. Clast size, density, and compositional variation can be clearly discerned using the CT data. The increase in clast size with depth in the suevite is reflected by an increase in variability of the average CT number with depth.

Unit 3 marks a slight drop in average CT number compared to Subunit 2C, and CT numbers remain constant, with some variability, through Subunits 3A and 3B. Texturally, Subunits 3A and 3B are very distinct in the CT data. Subunit 3A has a fluidal texture of intermixed light gray and dark gray material, whereas Subunit 3B is considerably more homogeneous and contains occasional clasts.

Lower peak ring

CT facies for Unit 4 were described during visual core description. There are several CT facies within Unit 4, all linked to the described lithology. In general, all of the lithologies within the lower peak ring section are easily distinguished on the basis of CT number, ρ_b, Z_{eff}, and texture.

Granitoids are easily identified in the CT data by their distinctive texture and the individual textures of the constituent minerals. Deformation to the granitoids generally corresponds to low ρ_b regions of the rocks. Pre-impact subvolcanic rocks are generally fine grained (although occasionally porphyritic); nonetheless, each of these units can be distinguished based on their CT number, ρ_b, and Z_{eff}. The suevites and impact melt rocks within the lower peak ring are distinctly different in the CT data from those found in the upper peak ring, and this difference is expressed primarily by their CT textures. In both locations, the suevites and impact melt rocks are easily distinguished from each other by the higher ρ_b and Z_{eff} of the impact melt rocks.

Biostratigraphy

Seventeen age-diagnostic biostratigraphic datums were identified at Site M0077, ranging from the middle Eocene to the base of the Paleocene. The Eocene section ranges from planktonic foraminifer Zone E7b to E5 and calcareous nannofossil Zone CP12 to CP10. Eocene sediments at Site M0077 are characterized by diverse but variable assemblages of both foraminifers and nannofossils and contains rare to dominant radiolarians, which are often associated with more organic-rich, laminated, and sometimes indurated lithologies that can only be examined in thin section. Benthic foraminifers are relatively rare and comprise an assemblage indicative of middle bathyal depths (500–700 m below sea level).

A set of stacked unconformities spanning Sections 36R-4 through 37R-1 (~606.5–607.5 mbsf) separate the Paleocene and Eocene sections and include several partial intervals of the upper Paleocene (including sediments spanning the PETM; nannofossil Zone CP8). The lower Paleocene appears to be complete and ranges from planktonic foraminifer Zone P3b to Pα. Nannofossil zonation is difficult in this interval, and the assemblage is dominated by bloom taxa (e.g., *Braarudosphaera*). *Thoracosphaera*, a calcareous dinoflagellate common in early Danian marine records, is very abundant at the base of the post-impact sediments. Below Zone Pα is a 40 cm brown siltstone that contains a number of Maastrichtian foraminifers and nannoplankton indicative of impact-related reworking and/or survivors.

Analysis of micro- and macrofossil material in the impact breccia reveals a diverse assemblage of Cretaceous organisms spanning the Early Cretaceous to the Maastrichtian that are indicative of a number of environments, from shallow-water carbonate platforms to open-shelf pelagic limestones.

Paleomagnetism

The primary goal of shore-based paleomagnetic studies was to produce a preliminary characterization of the NRM of post-impact sediments as well as suevite, impact melt rocks, and basement target rocks within the peak ring of the crater. This objective was achieved by conducting measurements of the NRM and limited alternating field (AF) demagnetization (up to either 15 or 20 mT) of discrete paleomagnetic specimens collected at a minimum frequency of ~1 sample per 3 m spanning the entire length of the Expedition 364 core.

The post-impact sedimentary column typically had NRM intensities between 1×10^{-10} and 8×10^{-9} Am^2 (for sample volumes of ~12.25 cm^3). The majority of sediment samples carried a normal polarity magnetic overprint that represents either viscous contamination from the geomagnetic field, drilling-induced magnetization, or some combination thereof. Because this magnetic overprint was not fully removed by AF demagnetization to 15–20 mT, the underlying detrital remanent magnetization could not be properly characterized during the expedition. Therefore, attempts to produce a polarity magnetostratigraphy and age model from the sedimentary column will be reserved for postexpedition analyses, when AF demagnetization to field levels higher than 20 mT are permitted.

Suevite and impact melt rocks within the core dominantly have NRMs of reversed polarity with a mean inclination value of approximately –44°. Some breccia samples exhibit a normal polarity magnetization of inclination of approximately 38° that was likely acquired after the impact. Both of these observations are consistent with prior paleomagnetic investigations of these lithologies in other locations within the Chicxulub crater. NRM intensities of the suevite are 3–4 orders of magnitude higher than those of the post-impact sediments. The impact melt rocks have the highest NRM values in the entire core, ranging between ~2×10^{-5} and ~2×10^{-4} Am^2.

Basement rocks within the core, which are primarily granitic and intruded by dikes, often have two magnetization components. For the vast majority of basement samples, NRM exhibits negative inclinations that are broadly consistent with the expected inclination at the time of the impact, which took place during reversed polarity Chron 29R. However, after AF demagnetization to 20 mT, the residual moment often exhibits a positive inclination. The NRMs of basement target rocks range between ~3×10^{-8} and ~4×10^{-5} Am^2.

Age model summary

Seventeen foraminifer and nannoplankton biostratigraphic datums were identified at Site M0077. Paleomagnetic reversal datums are excluded from the age model because of pervasive overprinting. The age-depth plot reveals that sedimentation rates vary widely throughout the section. The Eocene is characterized by high sedimentation rates, averaging 2.3 cm/ky, whereas the Paleocene is characterized by very low sedimentation rates, averaging 0.22 cm/ky.

The age model was applied to shipboard dry bulk density data to generate mass accumulation rates for Site M0077, including rates for organic carbon and bulk carbonate deposition. In general, organic carbon accumulation is highest in the younger Eocene section after rising from nearly zero at the base of the Eocene section; carbonate mass accumulation rate is generally high throughout but also increases from the base of the Eocene section to a peak around 50 Ma.

Geochemistry

Composition and abundance of major, minor, and trace elements, including carbon species and sulfur, and modal mineralogical compositions were measured on 246 samples from Expedition 364 cores. Samples were divided into three groups according to the lithostratigraphic division of the transected interval: (1) post-impact sediments, (2) suevite and impact melt rock, and (3) granitic basement. We analyzed 34 samples from the post-impact section from Cores 3R through 39R (506.2–604.3 mbsf), 50 samples from the impact breccia section from Cores 40R through 95R (619.4–744.1 mbsf), and 163 samples from the granitic section from Cores 96R through 272R (747.89–1237.03 mbsf).

Post-impact sediments are dominated by $CaCO_3$ with low SiO_2 content expressed as limestones, marlstones, and black shales. The upper post-impact sediment section is strongly enriched in organic carbon, which drops to very low concentrations in the lowermost 20 m of this unit. Details of XRF linescan and uXRF mapping of Section 40R-1 show localized enrichments in Ni and Cr near the boundary between limestones and suevite. This boundary also shows a significant change in composition from calcium carbonate–dominated to silicate-dominated lithologies. The suevite and impact melt rock section from 619.4 to 744.1 mbsf can be divided into three subsections based on the homogeneity and compositions of sample intervals. An upper subsection of suevite is characterized by a relatively homogeneous composition, which is succeeded by a lower suevite section that exhibits pronounced scatter in the determined elemental concentrations. The impact melt rock section at the bottom of the suevite lacks the high carbonate content of the two suevite sections above and shows higher content of silicate mineral component–derived element concentrations, such as Si, Al, K,

Na, V, Rb, and Zr. Organic carbon contents are very low in the suevite and impact melt rock section, and total carbon contents are dominated by carbonate carbon.

The granitic basement section shows relatively homogeneous concentrations of major, minor, and trace elements that are dominated by SiO_2 but yielded surprisingly low total concentrations. The monotonous granitic chemical character is punctuated throughout the section by intercalations of suevite, impact melt rocks, and subvolcanic rocks that display variable compositional characteristics. Generally, total organic carbon concentrations are similarly low in the granitic basement section compared to the suevite and impact melt rock section; however, carbonate-related carbon contents are markedly lower.

Physical properties

Physical property measurements were acquired from all cores recovered during Expedition 364. Offshore measurements were taken on whole-round cores (gamma density, electrical resistivity, magnetic susceptibility, and natural gamma ray), and onshore measurements were taken on half-round cores (color reflectance and thermal conductivity) and on discrete samples (*P*-wave velocity and moisture and density). Measurements are overall of good quality and reflect the different lithostratigraphic units. *P*-wave velocity, resistivity, magnetic susceptibility, and natural gamma ray were measured both on cores and downhole, and the two data sets correlate well (Figure **F12**).

In the post-impact sediments, porosities decrease with depth, densities and *P*-wave velocities increase, and magnetic susceptibility and natural gamma ray remain relatively constant with low values.

In the upper peak ring, *P*-wave velocities and densities are low compared to the overlying post-impact sediments, but both properties increase with depth. An opposite trend is observed for porosities. The post-impact sediment to peak ring contact is marked by an abrupt increase in the magnetic susceptibility and natural gamma ray signals.

Finally, in the lower peak-ring rocks, *P*-wave velocities increase with depth, with local excursions associated with dikes. Overall, densities remain constant except for local abrupt changes in the dikes or in the lowermost 100 m of the hole, where values decrease. Porosity values remain constant through the lower peak-ring rocks and start increasing in the lowermost 100 m of the hole. Natural gamma ray and magnetic susceptibility are constant overall in the lower peak-ring rocks, with clear positive or negative excursions in the dikes.

Downhole logging

The set of downhole geophysical tools used during Expedition 364 was determined by the scientific objectives, drilling/coring technique, hole conditions, and temperature at the drill site during operations.

Wireline logging and VSP data were acquired in three logging phases: upper interval at ~0–503 m DSF, middle interval at ~506–699 m DSF, and lower interval at 700–1334 m DSF. In the lower interval, wireline logs were acquired in two steps to avoid an interval of potential hole instability (mud circulation loss zones), identified as Lower A (939 m DSF to total depth) and Lower B (935–701 m DSF) intervals (Figure **F13**). The following measurements were acquired in three stages using slimline tools: spectral and total gamma radiation, sonic velocity, acoustic and optical borehole images, electrical resistivity, induction conductivity, magnetic susceptibility, caliper, borehole fluid parameters, and seismic traveltime versus depth from the VSP (Figures **F13**, **F14**). Logs were recorded either with standalone logging tools or with stackable tools, combined into tool strings, which were lowered into the hole after completion of coring operations over a given interval. For the first time in IODP, Expedition 364 deployed stackable slimline probes.

The majority of measurements were performed in open borehole conditions (no casing). The recovery and overall quality of the downhole logging data are good due to the excellent borehole conditions (Figure **F13**), although some of the logs have a poorer quality in the upper part of the hole (~0–400 m wireline log depth below seafloor [WSF]) due to a wider diameter and imperfect borehole conditions. At the scale of the borehole, resistivity and sonic logs are well correlated, as expected. The wireline logs are also in good agreement with the physical properties data acquired both on whole-round cores and on discrete samples (Figure **F12**).

In the post-impact sediments (0–616.7 m WSF), resistivity from induction log (Res from IL) gives a mean value of 1.2 Ωm, mean *P*-wave sonic velocity (V_P) is 2800 m/s (below 460 m WSF), and magnetic susceptibility is low, $<30 \times 10^{-5}$ SI, as expected in carbonates. The character of the gamma ray log changes downhole with a major step in the base level at ~274 m WSF, with a mean value around 100 API in the upper interval and of ~30 API in the lower one. The transition to suevite is found at 616.7 m WSF and characterized by a major change in the wireline log properties observed ~0.65 cm below, at 617.35 m WSF, and illustrated by a sharp downhole decrease in *P*-wave sonic velocities and induction resistivity and an increase in gamma ray.

In the upper peak-ring interval (616.7–746.2 m WSF), a clear change in log pattern is observed at ~705.5 m WSF, ~17 m above the top of the impact melt rock found in cores at 722 mbsf. From ~616 to 705.5 m WSF, in the suevite, the logs show low variability. The induction resistivity log gives an average value of ~2.6 Ωm. Resistivity and sonic logs follow the same trend. Average sonic *P*-wave velocity is ~2900 m/s. Magnetic susceptibility is low, below 260×10^{-5} SI. The gamma ray log shows low variability with an average of 80 API. From ~705.5 m WSF to the base of the impact melt rock at 746.2 m WSF, the wireline logs show much higher variability compared to the suevite above. The average resistivity is 3.6 Ωm and the average sonic *P*-wave velocity is ~3900 m/s, ~1,000 m/s higher than the suevite above. Magnetic susceptibility is high with an average of 1000×10^{-5} SI. The gamma ray log shows values ranging between 32 and 260 API. The contact between the impact melt rock and the basement below is found at 746.2 m WSF and marked on the wireline logs by a sharp decrease in magnetic susceptibility and an increase in gamma ray.

In the lower peak-ring interval (746.2–1334.69 m WSF), wireline logs are characterized by moderate to low variability. Mean resistivity is ~5 Ωm, and average sonic *P*-wave velocities are ~4100 m/s. Magnetic susceptibility is generally low (<0.002 SI) with increasing values in the impact melt rock and suevite intervals. Gamma ray in the granite provides consistent values of ~250 API whereas higher values (>400 API) are observed in the suevite.

At the borehole scale, the borehole-fluid temperature increases progressively downhole from ~26°C to 66.5°C at the base of the hole, and the borehole fluid conductivity ranges from 55,000 to 240,000 µS/cm. The measurements were acquired in several phases shortly after the drilling; hence, fluid parameter logs should only be used qualitatively. The borehole-fluid temperature likely reflects a minimum value for the in situ temperature of the formation, whereas borehole conductivity is affected by recent drilling opera-

tions and the presence of drill mud and seawater in the hole. Acoustic borehole images are mostly of good quality and should allow reorientation of the majority of cores with respect to magnetic north. Figure **F15** illustrates the deviation of Hole M0077A.

The three-component VSP is characterized by four major velocity regions, each with velocity increasing with depth (Figure **F14**). In the post-impact sediments, the boundary between Zones 1 and 2 is marked by 300 m/s increase in velocity and 10 m/s decrease in velocity uncertainty. An increase in velocity and increase in uncertainty (400 and 17 m/s, respectively) are seen at 595 m WSF with the transition to suevite. The most prominent velocity increase is seen at the impact melt rock contact and continues in to the granites with a jump of more than 1100 m/s.

Microbiology

Asteroid and comet impacts are known to cause severe disruption to surface biota, as is the case for Chicxulub, but what is their effect on the present and ancient deep biosphere, where a large proportion of Earth's biomass resides? Rock samples from every 3 to 9 m (post-impact sediments) and 9 m (upper and lower peak ring) were obtained aseptically directly upon coring and prepared for anaerobic cultivation and cell enumeration as well as for cultivation-independent metagenomic taxonomic and functional diversity profiling. Specific questions that will be addressed for the study of the present day biosphere follow: How does biomass change with depth? Which microbes are there and what are they doing? It is hypothesized that once the impact-induced hydrothermal system cooled, conditions improved to support deep subsurface recolonization. The brecciated regions within impact craters are of particular interest because the heavily fractured, brecciated rock is likely to lead to an increase in fluid flow and the availability of nutrients and redox couples to microbiota. Another objective is to study the ancient deep biosphere within the recovered core. For this project, we will explore to what extent ancient plankton DNA can be recovered from Cenozoic marine sediments overlying the Chicxulub impact crater and whether this DNA is suitable for study of the post-impact recovery and development of marine life. In addition, we will explore to what extent slow growing and presumably slowly evolving bacteria and/or archaea in the Cenozoic record can provide information about post-impact environmental and depositional conditions. The parallel analysis of the composition of fossil lipid biomarkers and their isotopic compositions will provide information about the source and bioavailability of organic matter and provide additional proxies for establishing the paleoenvironmental conditions that prevailed at the time of deposition such as trophic status, euxinia, ocean acidification, changes in hydrological balance, and atmospheric CO_2 concentrations. For example, the paired analysis of more recalcitrant lipid biomarkers could reveal whether life has been present in the past in the case that the more labile nucleic acids and/or microbial cells are below the detection limit.

Offshore operations

All times are reported in Central Daylight Time (CDT).

Mobilization of the drilling platform

Mobilization of the drilling platform, the *L/B Myrtle*, was undertaken in several phases. The vessel is a liftboat with a shallow draft and limited sailing weather window (fair weather). The drilling system was to be cantilevered over the bow of the *L/B Myrtle*, and the vessel could not sail with the drilling rig in this position. Therefore, it was not possible for the vessel to be fully mobilized until the platform had reached the drill site.

Between 12 and 13 March 2016, the first mobilization took place at the port of Fourchon, Louisiana. The drilling system was sourced from DOSECC (Salt Lake City, Utah [USA]), and the containerized laboratories and downhole logging equipment were brought in from various European countries and Canada. All the equipment was placed on board, along with the laboratories, offices (including IT and database), and refrigerated and drilling containers. These were secured into working positions but not powered, networked, or set up for operations. The inner part of the cantilever platform, the drill ancillary equipment, and the various drill tubulars were positioned and secured. The outer part of the cantilever, the drill, and the generators were stowed inboard and away from the wash of the bow for the transit.

On 15 March, the *L/B Myrtle* sailed from Port Fourchon heading toward Progreso, Mexico, via Brownsville, Texas (USA). This class of liftboat is only authorized to sail in water depths it is able to jack up in, so it took a route around the Gulf of Mexico, passing close to the coast of the US and Mexico. Poor weather slowed progress to Brownsville, requiring the *L/B Myrtle* to halt and jack up several times and wait out the weather.

On 22 March, the *L/B Myrtle* arrived at the port of Brownsville, refueled, and cleared customs. Poor weather and technical issues delayed the departure until 27 March, when the second phase of transit to the port of Progreso commenced with several more stops for weather.

On 4 April, the *L/B Myrtle* arrived at the port of Progreso. After clearing the formalities of the port, the ESO team and the drill crew joined at 1500 h. The cantilever was fitted prior to leaving port because this process is more readily achievable when positioned quayside than when the vessel is jacked up at sea.

Transit to Hole M0077A

At 1300 h on 5 April 2016, after fuel, food, and drilling mud were loaded, the *L/B Myrtle* set sail from the Port of Progreso and headed for the drill site (Hole M0077A). At 1530 h, the *L/B Myrtle* arrived on site and prepared to position above the hole.

At 1544 h on 5 April 2016, the *L/B Myrtle* was positioned above Hole M0077A and the legs were lowered to the seabed. The seabed was tagged at 1551 h, and the leg preload procedure began. The preload and settlement procedure continued until 0700 h on 6 April, when the *L/B Myrtle* jacked up to ~13.1 m above sea level. Following completion of the required health and safety drill, access to the working deck was granted and final mobilization of the drilling rig and ESO laboratories commenced. At 1940 h, the supply vessel *Linda F* arrived at the platform and delivered drilling mud. Mobilization continued throughout 7 April with a visit from the *Linda F* at 1300 h for a vessel crew change and some additional supplies. At 1900 h, drilling operations commenced with running the conductor pipe to the seabed.

Hole M0077A

At 0330 h on 8 April, the conductor pipe reached the seabed, and preparations for open-hole drilling were made. An open-hole assembly comprising a 12¼ inch tricone bit was utilized. At 1342 h, the drill reached the seabed and drilling began. Drill cuttings were collected at regular intervals from mud returned to deck via the temporary guide casing. At 1550 h, a depth of 15.5 m DSF was reached and the pipe was tripped out to start running the 9⅝ inch casing into the hole. At 0045 h on 9 April, the conductor casing was

in place and cement was injected into the hole and allowed to set. At 1500 h, casing was cut to length and the mud diverter system was set up on the drill floor. Next, a 7⅞ inch tricone bit was run in to the top of the cement, and open-hole drilling commenced with a target depth of 500 m DSF. Cuttings were collected from the mud recycling system with every 5 m advance downhole.

Drilling continued on 10 April at a rate of approximately 8 m/h. Between 82 and 101 m DSF, mud circulation was lost and, following attempts to adjust mud composition in order to counteract this loss, the decision to cement the hole was made. Following cementation, 24 h were allowed for the cement to cure. At 0000 h on 12 April, pipe was run in, and at 0435 h, drilling of the cement plug at 82 m DSF commenced. Despite a further loss of circulation in this section, drilling progressed, reaching a depth of 229 m DSF by 2400 h. During 12 April, the supply vessel visited the *L/B Myrtle* once again, delivering ESO personnel, logging engineers, food, and fuel.

Drilling continued during 13 April, achieving target depth for open-hole drilling at 503 m DSF at 2153 h. The remainder of April 13 was spent pulling out of the hole and preparing for downhole logging operations and vertical seismic profiling.

At 0955 h on 14 April, test firing of the air gun occurred, accompanied by appropriate marine mammal and protected species observation. At 1015 h, the supply vessel arrived and ESO personnel and members of the Science Party joined the *L/B Myrtle*.

At 1300 h, wireline logging commenced. By 1600 h, all logging tools were recovered to deck to ensure VSP operations were carried out in daylight. The VSP continued until 2330 h and was preceded and accompanied by appropriate mammal and protected species observations. The VSP was recovered at 2400 h on 14 April, and the setup for wireline logging commenced. Logging operations continued throughout 16 April until 1400 h.

Following this, the drill string was tripped and casing was run into the hole. Running casing continued until 2400 h, during which difficulties with connecting the casing were noted. In order to assess the condition of the casing, downhole logging was carried out at 0215 h on 16 April. This process included running the EM51 and the QL40-SGR (spectral gamma) + QL40-ABI40 (acoustic televiewer) tool string. Based on the results, it was considered possible to continue casing by connecting two pipes downhole, and the full depth of the open hole was cased by 2000 h. Following this, the hole was cemented and left to cure.

On 17 April at 1300 h, running of pipe commenced to remove cement from the base of the hole and start coring. Cement was encountered at a shallower depth than anticipated, and at 1820 h, the core barrel became stuck. After attempts to free the core barrel, the string was tripped at 2000 h. This process continued until 0040 h on 18 April, when the bottom-hole assembly (BHA) was recovered to deck. The rubber bung used to push the cement was caught in the BHA and identified as the obstruction preventing further progress. After changing out the BHA, pipe was run back into the hole. However, an obstruction was again encountered at the same depth (307 m DSF) where the casing was reconnected downhole, indicating potential misalignment of the casing. At 0825 h, it was necessary to once again trip the pipe in order to add a reaming bit to the BHA so that milling and reaming could be carried out to advance through the casing. Running in of pipe recommenced at 1500 h, and at 0710 h on 19 April, the milling and reaming assembly reached the base of the hole and was tripped out to make preparations for coring.

At 1315 h on 19 April, the coring assembly was prepared and running in pipe recommenced. At 2020 h, the BHA was recovered for inspection and was then de-latched and sent back to the bottom of the hole. Due to lack of progress, the string was again tripped out at 2043 h. A modification was made, with a fabricated "stinger" added to the BHA to guide it past the misaligned casing. This assembly was run in at 0345 h on 20 April. By 0655 h, the BHA had passed the misaligned casing and progressed to the base of the hole, where coring commenced. At 1055 h, the barrel was recovered to deck. It contained debris material associated with the drilling process (metal and rubber). A second core barrel was deployed and rotated for approximately 30 min with no advance. On recovery to deck, this barrel was found to be empty. Following discussion, it was decided to fish for any further pieces of metal (thought to be crowns from a damaged bit) which could be down the hole. Attempts to remove debris and advance coring were made throughout the day.

On 21 April, attempts to remove debris continued until 1415 h, when essential maintenance to the rig was carried out. Maintenance of the rig continued throughout the day until 0710 h on 22 April. For the remainder of the day, attempts to clear the borehole of debris continued. At 2330 h after no advancement, the pipe was tripped to change the bit.

Tripping of pipe continued until 1155 h when the BHA was recovered on deck. A tricone bit was added to the BHA to drill open hole past the obstruction. Shortly afterward, the *Linda F* arrived to transfer personnel to the platform. Running in pipe continued, and at 1630 h, open-hole drilling commenced. By 2120 h, 505.70 m DSF had been reached, advancing the hole beyond the debris/obstruction.

Tripping of the pipe commenced and continued into 24 April until 0215 h, when the BHA was recovered to deck and the bit changed to allow coring. The pipe was run in and reached the base of the hole at 0730 h, when coring commenced. The first core, Core 1R, was recovered to deck at 0800 h. Coring then continued throughout 24 April with a total of nine runs, reaching 521.67 m DSF.

During the early hours of 25 April, it was necessary to carry out maintenance on the top drive motors, resulting in a break in coring until 0505 h. Cores 10R and 11R were recovered at 0650 and 0900 h, respectively, before further rig maintenance was required. Coring then progressed smoothly throughout 25 April, reaching 546.09 m DSF by 2400 h.

The supply boat arrived at 1600 h on 26 April to deliver groceries and other supplies. Smooth coring operations continued throughout 26–28 April, recovering a total of 41 cores (17R–58R), all of which were high quality, maintaining core diameter with few breaks and high recovery. The total distance advanced over this period was 128.1 m to 674.19 m DSF.

At 0500 h on 29 April, after recovering Cores 59R and 60R, changes in drilling parameters were recorded and the pipe was tripped to assess the condition of the BHA and drill string. On recovery, the bit was worn and was therefore changed before running in commenced. Coring started at 2300 h, and Core 61R was recovered to deck by 2355 h.

Coring continued throughout 30 April. Due to a change in lithology and in order to optimize recovery, core runs were shortened to ~1.5 m on average and the coring rate was reduced. By the end of the day, a total of 11 core runs (Cores 62R–72R) were completed, advancing the hole 15.75 m and reaching 699.09 m DSF. Core recovery averaged 81%.

On 1 May, essential maintenance of the rig was carried out for the majority of the morning. Once complete, the core barrel was recovered to deck, and it was found that the core catcher contained a "stub" of core, probably left behind by the previous run (Core 72R).

A decision was made to trip the pipe the step down to standard PQ3 drill string, allowing the next phase of the downhole logging program to commence.

Set up for logging commenced, and the pipe was tripped to 507 m DSF, just below the depth of casing, to enable open-hole logging.

Logging operations continued for the remainder of the day, and logging personnel were transferred to the platform on the *Linda F*. The first tool run downhole was the induction magnetic susceptibility standalone tool, followed by a tool string comprising the spectral natural gamma ray, sonic, and fluid and temperature conductivity tools, run from ~698 to 507 m WSF. Toward the end of the day, a tool string comprising the spectral natural gamma ray tool, caliper, and acoustic borehole imager was sent down the hole. Downhole logging operations continued during the early hours of 2 May. The tool string, as outlined above, was run uphole from ~697 m WSF at very high resolution. While rig-up for VSP operations was ongoing, marine mammal and protected species observations were carried out. Following technical issues with the depth encoder, the VSP tool was lowered to 696 m WSF and run uphole at a high resolution. Marine mammal and protected species observation continued during and after VSP operations. Upon completion of downhole logging operations, maintenance of the drill rig continued for the remainder of the day. The *Linda F* arrived, and logging personnel disembarked.

On 3 May, maintenance of the drill rig was complete and running in pipe began. The base of the hole was reached at 0325 h, and coring commenced. On recovery of Core 73R, fragments of the drill bit were found in the core liner, indicating the bit had worn in places. The pipe was therefore tripped to recover the BHA for inspection. Following discussion, the decision was made to case and cement the borehole and step down to a standard PQ3 size drill string to improve coring efficiency. Casing of the hole started and continued through the remainder of the day. The total depth reached using oversized PQ3 size drill string was 701.64 m DSF. During the day, the *Linda F* arrived to transfer supplies and personnel.

Running casing continued until 0510 h on 4 May. The casing was set by pumping cement to the base of the hole and allowing up to 12 h to cure. To maximize operational time while the cement was curing, a wireline tool sting comprising the natural gamma ray tool and acoustic imager was sent downhole. Upon completion of the downhole logging exercise, the drill string was run into the hole in preparation for coring; this continued for the remainder of the day.

Running pipe continued until 0230 h on the morning of 5 May. Upon reaching the base of the hole, coring of the cement began with a cement core being recovered at 0329 h. Coring continued throughout the day and was intermittently interrupted to carry out essential maintenance on the drill rig. Coring runs were kept short to maximize recovery in challenging lithologies. A total of seven cores were recovered throughout the day, advancing the hole by 5.7 m. Core recovery was 100%, and quality was good. By midnight, coring reached 707.34 m DSF and continued.

On 6 May, coring continued throughout the day, with a total of nine cores recovered. The recovery rate was an improvement on the previous day, and the quality of the core was very high. The hole was advanced by 21.35 m, reaching 728.69 m DSF.

Coring continued with rates continuing to increase as the lithology became more competent. The recovery and quality of the cores remained high, and the hole was advanced by 24.40 m to 753.09 m DSF by the end of 7 May.

Coring continued to progress throughout 8 May. In general, the recovery and quality of core remained high. The only exception was while drilling Core 99R, when the bit became blocked, and as a result, a short run was recovered. The core was blocked in the tube with many fractured pieces and was difficult to extract. However, following this, coring resumed with excellent recovery rates and high-quality cores collected. A total of 11 cores were collected, reaching 783.59 m DSF.

The high-quality recovery continued throughout 9 May. While running Cores 117R and 119R, the bit became blocked again, which resulted in shorter core runs. All other cores were full 3.05 m runs, with a total of 28.35 m recovered from 11 cores.

Coring continued throughout the morning of 10 May. While drilling Core 123R, a loss of circulation was noted at ~821 m DSF (~5% mud loss). As a result, loss circulation material was pumped down the hole followed by drilling mud, which resolved the issue, and coring resumed. Following several unsuccessful attempts to core, the drill string was tripped to recover a suspected worn bit. The BHA was recovered at 1544 h, and the worn bit was replaced. The pipe was then run back in, and coring recommenced at 2145 h.

Two cores of excellent quality and 100% recovery were recovered by 0340 h on 11 May. Following this, several attempts were made to core further, but there was no advancement. A decision was made to trip the drill string, commencing at 0850 h, in order to inspect the BHA. The BHA was recovered, and the bit was replaced. Pipe was run back into the hole, and coring recommenced at 2010 h. However, the core run was short because the bit blocked off due to a crumpled liner. As coring continued, the hole depth at midnight measured 830.09 m DSF, an advance of 6.85 m from the previous day.

Coring initially progressed slowly without interruption on 12 May. Four cores were recovered during the morning (by 1155 h) and a further three during the afternoon. The cores continued to be high quality, and a 100% recovery rate was achieved. The day finished with the hole advanced by a further 17.30 m to 847.54 m DSF.

On 13 May, coring continued from the previous day. While coring Core 136R, the barrel became blocked, and the run was recovered early. Despite torque remaining steady and mud flow constant, no penetration was made on a further attempt to core, and it was concluded that the bit was worn. As a result, the majority of the morning and early afternoon was spent tripping out/in the hole and replacing the bit (0400–1230 h). Coring commenced at 1230 h with short (0.4–0.7 m) cores recovered initially. The final two cores of the day (140R and 141R) were recovered following full runs, measuring 3.10 m each. The final hole depth at midnight was 859.54 m DSF.

At 0000 h on 14 May, a motor change on the rig was carried out during shift changeover, and coring recommenced at 0055 h. Coring continued steadily throughout the day, with a total of 11 cores collected, which advanced the hole depth by a further 30.80 m. These cores were very high quality with 100% recovery. The hole depth at the end of the day was 890.34 m DSF.

On 15 May, coring continued with high-quality cores retrieved at a recovery rate of 100%. Rig maintenance (repair to a hydraulic hose) was required prior to the recovery of Core 156R at 0720 h. Once complete, coring recommenced at 0855 h and continued for the remainder of the day. At the end of the day, the hole depth was 926.94 m DSF with a total of 14 cores (36.60 m) recovered.

Coring continued throughout the day on 16 May. The changes in formation slowed progress for short periods of time, and a loss circulation zone caused a small delay in drilling as loss circulation material was prepared and delivered downhole. However, due to continued loss of mud, a higher ratio of water to mud was adopted to preserve the mud supply. Cores were again of extremely high

quality with 100% recovery and a steadily improving coring rate. By the end of the day, 14 cores totaling 36.60 m had been collected, which advanced the hole depth to 963.54 m DSF.

The coring rate continued to increase throughout 17 May with a total of 17 cores (51.85 m) recovered over the 24 h period, taking the hole depth to 1015.39 m DSF. Due to a continued loss of circulation relating to issues from the previous day, water and dilute mud were used to flush the drill cuttings.

On 18 May, coring continued without any stoppages: 15 cores were collected (42.13 m in length), furthering the hole depth to 1057.52 m DSF. Toward the end of the day, issues were noted with the barrel failing to latch in. Once latched in and lowered to ~10 cm from the base of the hole, pressure increased to an unworkable level (300–500 psi) while torque remained low (less than 1000 psi). It was concluded that the bit had worn, and as a result, the majority of the late morning and early afternoon on 19 May was spent tripping pipe out of the hole. The bit was then replaced, and coring recommenced at 1415 h, producing high-quality cores with 100% recovery. The day ended with a hole depth of 1075.92 m DSF, following the retrieval of six cores measuring 18.40 m in total.

Coring continued uninterrupted throughout 20 May. Cores were excellent quality, and 100% recovery was achieved. The day ended at 1121.64 m DSF, having drilled 45.72 m in total. Coring continued to progress without any maintenance stoppages throughout 21 May (ending at 1166.19 m DSF, having drilled 44.50 m) and into 22 May.

Coring continued throughout 22 May with excellent quality cores with close to 100% recovery. The day ended at 1215.24 m DSF, having drilled 49.05 m (16 individual cores).

Coring continued from the previous day, and progressed uninterrupted throughout 23 May. Cores were excellent quality, and 100% recovery was achieved. The day ended at 1255.54 m DSF, having advanced the hole by 40.30 m (13 cores).

Throughout 24 May, coring continued uninterrupted. The 12 cores collected were consistently high quality, and the day ended with a hole depth of 1291.29 m DSF.

On 25 May, there were no operational issues and coring proceeded continuously with the same high quality and recovery rates. The day ended at 1328.49 m DSF, having advanced the hole by 37.20 m. A total of 12 cores were recovered.

The final cores of Expedition 364 were collected on 26 May. The final two cores collected were again of excellent quality and 100% recovery. The final hole depth for M0077A was 1334.69 m DSF attained at 0235 h, having advanced the hole by 6.20 m since midnight.

With the completion of coring on 26 May, the supply boat *Linda F* transferred the Science Party to Progreso, leaving the ESO and DOSECC staff and Montco crew on board the *L/B Myrtle*. The hole was flushed with water, and pipe was pulled in preparation for downhole logging activities. Wireline logging tools were run from the bottom of the hole (1334.69 m DSF) to ~940 m DSF (Lower A logging interval) at 0740 h. Initially, the electrical resistivity tool was run, followed by a tool string comprising the gamma ray, sonic, and borehole fluid probes. The acoustic borehole images and caliper and spectral gamma ray logs were successively acquired between 1620 and 2308 h. All data were of good quality.

Downhole logging operations proceeded on 27 May with the acquisition of gamma ray, caliper, and optical images from ~1046 to ~940 m DSF because the elevated bottom hole temperature inhibited the tool from working properly at depth. Following the tripping out of pipe, wireline operations recommenced at 0740 h with electrical resistivity, followed by a tool string comprising the gamma ray, sonic, and borehole fluid probes. Centralized tools were not run across the interval at which mud was lost (~940 m) to avoid destabilizing the borehole wall. The third tool run at 1143 h consisted of the gamma ray, caliper, and acoustic imager tool string. At ~850 m DSF, the borehole diameter expanded beyond the size of the centralizer. The tool string was pulled back to deck at 1612 h, and centralizers changed for larger ones. After completion of the logging phase for the Lower A interval, the magnetic susceptibility and induction standalone tool was run. The tool string containing the acoustic imager was sent downhole again at 1840 h to image the ~940–700 m DSF interval. A tool string comprising the gamma ray tool and fluid temperature probe was then sent to the bottom of the hole at 2350 h. All data were of good quality.

During 28 May, gamma ray and optical imager logs were collected. The tool string arrived back at the drill floor at 0630 h, and rig-up for VSP commenced. Marine mammal observations commenced in advance of VSP activities and continued throughout. The VSP tool was sent to the bottom of the hole, and data acquisition began at 0900 h. Acquisition was completed at 1340 h, and logging operations ended, clearing the drill floor at 1530 h. With the exception of the optical images, all data were of good quality. The recorded optical images were not consistent with the expected facies variations, likely due to the presence of mud cake. It is likely that the wider spacing between the borehole wall and casing at this depth resulted in a reduced fluid velocity when the borehole was flushed, and this condition led to less mud being removed. Once these final operational activities were complete, demobilization commenced at 1530 h and continued throughout the remainder of the day and through 29 May.

On 30 May, the *L/B Myrtle* successfully jacked down while all personnel were restricted to the uppermost deck in line with safety protocol. Following a short (approximately 3 h) transit, the *L/B Myrtle* arrived at the port of Progreso and the remaining crew (DOSECC and ESO staff) disembarked, ending the offshore operational phase of Expedition 364.

The cores, contained within the reefer (refrigerated container), continued onto Port Fourchon, Louisiana, onboard the *L/B Myrtle* (via US customs in Brownsville), arriving on 13 June. The reefer was unloaded on 14 June and was delivered to Weatherford Laboratories (Houston, TX [USA]), by truck on 15 June where the cores underwent CT scanning. Following completion of the CT scanning, the cores were repacked into the reefer and transported from Houston to the Port of Houston by truck on 13 July. Between 16 July and 6 August, the reefer was transported by ship to Bremerhaven, Germany. On 9 August, the reefer arrived at Bremen Core Repository, MARUM (Center for Marine Environmental Sciences, University of Bremen, Germany), in advance of the Onshore Science Party.

Preliminary scientific assessment

The goals of Expedition 364 in drilling the peak ring of the Chicxulub impact crater included achieving some specific tasks: to determine the nature and composition of the peak-ring rocks; to record the sedimentology and stratigraphy of the Paleocene–Eocene Chicxulub impact basin infill; to report the chronology of the post-impact fill, peak-ring rocks, and impact lithologies; to measure the petrophysical properties downhole and on the core; and to use these data to calibrate geophysical models.

We recovered core through the peak-ring rocks and found them to comprise fractured granitic basement covered by impact melt

rock and suevite. The post-impact interval comprises a mix of lithologies, including marlstones, claystones, limestones, siltstones, and black shales, constrained biostratigraphically to be deposited between ~49 and 65.5 Ma. Samples were taken for postexpedition research to perform Ar/Ar and U/Pb dating. A suite of wireline logs and multisensor core logger data was acquired; these data will now be used to groundtruth and improve geophysical models of the crater.

Additionally, the Expedition 364 goals can be grouped into three sets of key questions. These include questions surrounding the K-Pg extinction event and recovery of life, the subsurface habitability of impact craters, and the processes that form peak rings and weaken target rocks during large impacts.

In terms of the linkage between the Chicxulub impact and the end-Cretaceous mass extinction event, three key questions are what caused the environmental changes that led to a global mass extinction? What insights arise from biologic recovery in the Paleogene, within a potentially "toxic" ocean basin? And, can we constrain the volume of dust and climatically active gases released into the stratosphere by this impact using the recovered cores? Additionally, we sought to recover the climate signature of particular warm intervals within the post-impact sediments and generally investigate the infilling of the Chicxulub impact basin. The clast lithology within the suevites that make up the upper peak ring can be examined for evidence of depth of exhumation that may provide insight into volatile contribution to the atmosphere by the impact event. The lower Paleocene is relatively condensed but complete, with fossils indicative of planktonic Biozones P0 to P4. These initial results suggest that we will be able to address questions about the recovery of life in the ocean basin and directly compare the recovery with the evolving ocean chemistry. Nannofossils indicate that the PETM is present at Site M0077 bracketed by unconformities, and the Eocene section above is relatively thick.

In terms of the deep biosphere within the impact crater, we ask what effect does a large impact have on the deep subsurface biosphere, and can impacts generate habitats for chemosynthetic life? How long did an impact-induced hydrothermal system exist, and what is the relationship between hydrothermal processes and habitability of the impact crater? Cell counts and DNA in the peak-ring rocks indicate the presence of modern microbial life, suggesting impact breccias provide an ecological niche. This possibility is now being confirmed with additional tests. Hydrothermal minerals are commonly observed in the peak-ring rocks, demonstrating that hydrothermal processes were active after this impact.

Lastly, in the study of impact processes generally, we ask how are rocks weakened during large impacts to allow them to collapse and form relatively wide, flat craters? What rocks comprise a topographic peak ring, and how are peak rings formed? The fact that the peak ring is formed from uplifted, shocked, fractured basement rocks that overlie Mesozoic sediments (as observed in seismic reflection data) demonstrates that the dynamic collapse model for peak-ring formation is substantially correct (Morgan et al., 2016). Deformation of the peak-ring rocks includes brittle fractures, cataclasites, and pervasive shearing with slickensides that often crosscut each other. These observations will be used to address the kinematics of peak-ring formation and the weakening mechanism that governs impact crater formation during large impacts. The physical properties of these rocks demonstrate that the impact process reduces the density and velocity of target rocks and greatly enhances porosity. Additionally, peak rings can be viewed as sampling lithologies present within the crustal column, thus providing insight in planetary crustal composition using remote sensing.

In summary, the nearly 100% core recovery, high quality of the recovered core, completeness of the early Paleocene, and the successful wireline logging campaign at Site M0077 represent a great success. We are confident that the data acquired during Expedition 364 will accomplish the goals of the expedition and go a significant way toward answering the many questions posed about the impact crater, the end-Cretaceous mass extinction, and the effects of impacts on the deep biosphere.

Outreach and communication

The overall aim of the ESO Outreach and Education effort is to promote the benefits of each expedition's science, and the wider objectives of ECORD/IODP, to a broad audience, including the science community and public. To accomplish this objective, we focused on publicizing the expedition's aims and findings to international media and concentrated on media networks developed within the IODP/ECORD community and members of the Science Party's organizations. The approach is described in the Expedition Communications Plan, which was prepared by the ESO Outreach Managers, Co-Chief Scientists, and Expedition Project Manager, and distributed to all Science Party members prior to the expedition.

Targeted activities in support of the communication objectives included the following:

- The expedition web page on the ECORD website with links to documents such as the initial proposal and *Scientific Prospectus*. During the expedition, the website acts as a source of information from the offshore platform by including Ship Reports and blogs. A section on outreach provides links to the expedition materials and a media pack with information about press conferences and media releases, as well as contact details to arrange interviews with the expedition scientists.
- Expedition promotional materials, including an expedition logo, flier (in both English and Spanish), and branded items such as memory sticks, caps, T-shirts, and mugs for the Science Party members, ESO staff, and ship's crew.
- Banners with logos of ECORD, IODP, and ICDP and the expedition logo to display on the side of the offshore platform and onboard to act as a backdrop for interviews. Widespread use of logos ensures recognition in photographs/videos.
- Contact with media officers at the Science Party member's universities to raise awareness of their staff's participation in the expedition and to enlist their support in promoting the expedition locally and nationally.
- Engagement with the international media prior to the expedition and support for the organization of radio/media interviews.
- Organization of a media briefing at the start of the expedition in collaboration with the expedition's Mexican Scientific Coordinator, Professor Jaime Urrutia-Fucugauchi, expedition scientists Dr. Mario Rebolledo-Vieyra and Dr. Ligia Perez-Cruz, and communications staff at the Universidad Nacional Autónoma De México. The event was held at El Gran Museo del Mundo Maya in Mérida, Mexico, on 13 April 2016, where questions were put to Sean Gulick, Claire Mellett, Jaime Urrutia-Fucugauchi, Ligia Pérez-Cruz, Ricardo Bello Bolio, Director of Higher Education, Yucatan, and Eduardo Batliori Sampedro, Secretary of Urban Development and Environment. The media conference was at-

tended by about 40 media representatives, mainly from Mexican radio, TV, and print media; therefore, the event was conducted in both Spanish and English. The expedition received global interest and was reported in the US, Canada, Australia, and Mexico and in several countries in Europe and Asia. Interest in the expedition and the proximity of the platform to the Mexican coast led to a number of visits by media representatives and VIPs to the platform during the offshore phase of the expedition. A media day was organized on 23 April, when 24 media representatives/VIPs were able to visit the platform.

- The expedition was the first since the Arctic Coring Expedition (302) in 2004 to involve Education Officers both during the onshore and offshore phase. Educator and children's author Kevin Kurtz took part in both the onshore and offshore expedition and organized a Reddit AMA (Ask me Anything) event on 13 May in collaboration with the US Science Support Program (USSSP) and the University of Texas at Austin (USA; 2800 participants and 400 comments and questions). A Reddit AMA session was also organized for the onshore party, which took place on 10 October with more than 2000 participants and during which around 300 questions were asked.
- Teacher Barbara Matyssek and Kevin Kurtz contributed to the expedition blog and organized educational activities during a 2-week stay at the Onshore Science Party in Bremen. Matyssek conducted short interviews with eight scientists to be published on the ECORD website; questions dealt with the expedition's perspectives and the scientists' career paths. Kurtz arranged remote live events in the core repository for student groups and school classes. A total of 33 school classes and groups (1400 participants), mainly from the USA and Europe, took part in 26 sessions. As a long-term project, Matyssek and Kurtz will update a poster to be shown with K-Pg core replicas.
- A second media event was held during the Onshore Science Party on 11 October at MARUM and featured short presentations by the Co-Chief Scientists followed by interviews and tours of the laboratory facilities and core repository. The event was attended by representatives from Deutschlandfunk, Radio Bremen, Kreiszeitung, Planet Erde, and the BBC. The scientists' universities and institutions picked up the press release and published individual versions that resulted in features by various international media. Articles were published in newspapers and on online portals in the US, Mexico, Australia, Japan, and Europe (e.g., Austria, Germany, and the UK).
- Regular promotion of the expedition's accomplishments were posted on ECORD's social media platforms such as Twitter and Facebook. The ESO Outreach Facebook page reached an average of 2,000 visitors per day, peaking at 20,000 visitors on 7 May.
- An expedition blog (**https://esoexpedition364chicxulubimpactcrater.wordpress.com/about**) was maintained throughout the expedition (onshore and offshore) and included regular updates from both the offshore and onshore phases of the expedition. The blog received 5,982 views in April 2016 and 10,911 in May 2016, principally from the US, UK, Mexico, Germany, and France.
- Discussions with a television production company in late 2015 leading to an agreement to grant exclusive access to the expedition to make a TV documentary. A number of television production companies expressed an interest in making documentaries about the expedition, which may be followed up on after the exclusive agreement expires.
- Journalists working on "Asteroid Day" (**http://asteroidday.org**) asked British astronaut Tim Peake to take a photograph of the Chicxulub area from the International Space Station during the offshore phase of Expedition 364.

The expedition outreach efforts were successful in drawing significant international attention to the expedition on television and radio and in the written press.

References

Abramov, O., and Kring, D.A., 2007. Numerical modeling of impact-induced hydrothermal activity at the Chicxulub crater. *Meteoritics & Planetary Science,* 42(1):93–112. **http://dx.doi.org/10.1111/j.1945-5100.2007.tb00220.x**

Ames, D.E., Kjarsgaard, I.M., Pope, K.O., Dressler, B., and Pilkington, M., 2004. Secondary alteration of the impactite and mineralization in the basal Tertiary sequence, Yaxcopoil-1, Chicxulub impact crater, Mexico. *Meteoritics & Planetary Science,* 39(7):1145–1168. **http://dx.doi.org/10.1111/j.1945-5100.2004.tb01134.x**

Artemieva, N., and Morgan, J., 2009. Modeling the formation of the K–Pg boundary layer. *Icarus,* 201(2):768–780. **http://dx.doi.org/10.1016/j.icarus.2009.01.021**

Arz, J.A., Alegret, L., and Arenillas, I., 2004. Foraminiferal biostratigraphy and paleoenvironmental reconstruction at the Yaxcopoil-1 drill hole, Chicxulub crater, Yucatán Peninsula. *Meteoritics & Planetary Science,* 39(7):1099–1111. **http://dx.doi.org/10.1111/j.1945-5100.2004.tb01131.x**

Baker, D.M.H., Head, J.W., Collins, G.S., and Potter, R.W.K., 2016. The formation of peak-ring basins: working hypotheses and path forward in using observations to constrain models of impact-basin formation. *Icarus,* 273:146–163. **http://dx.doi.org/10.1016/j.icarus.2015.11.033**

Barton, P.J., Grieve, R.A.F., Morgan, J.V., Surendra, A.T., Vermeesch, P.M., Christeson, G.L., Gulick, S.P.S., and Warner, M.R., 2010. Seismic images of Chicxulub impact melt sheet and comparison with the Sudbury structure. *In* Gibson, R.L., and Reimold, W.U. (Eds.), *Large Meteorite Impacts and Planetary Evolution IV.* Special Paper—Geological Society of America, 465:103–113. **http://dx.doi.org/10.1130/2010.2465(07)**

Belcher, C.M., Hadden R.M., Rein, G., Morgan, J.V., Artemieva, N., and Goldin, T., 2015. An experimental assessment of the ignition of forest fuels by the thermal pulse generated by the Cretaceous–Palaeogene impact at Chicxulub. *Journal of the Geological Society,* 172(2):175–185. **http://dx.doi.org/10.1144/jgs2014-082**

Bell, C., Morgan, J.V., Hampson, G.J., and Trudgill, B., 2004. Stratigraphic and sedimentological observations from seismic data across the Chicxulub impact basin. *Meteoritics & Planetary Science,* 39(7):1089–1098. **http://dx.doi.org/10.1111/j.1945-5100.2004.tb01130.x**

Bryce, C.C., Horneck, G., Rabbow, E., Edwards, H.G.M., and Cockell, C.S., 2015. Impact shocked rocks as protective habitats on an anoxic early Earth. *International Journal of Astrobiology,* 14(01):115–122. **http://dx.doi.org/10.1017/S1473550414000123**

Christeson, G.L., Collins, G.S., Morgan, J.V., Gulick, S.P.S., Barton, P.J., and Wharton, M.R., 2009. Mantle deformation beneath the Chicxulub impact crater. *Earth and Planetary Science Letters,* 284(1–2):249–257. **http://dx.doi.org/10.1016/j.epsl.2009.04.033**

Claeys, P., Heuschkel, S., Lounejeva-Baturina, E., Sanchez-Rubio, G., and Stöffler, D., 2003. The suevite of drill hole Yucàtan 6 in the Chicxulub impact crater. *Meteoritics & Planetary Science,* 38(9):1299–1317. **http://dx.doi.org/10.1111/j.1945-5100.2003.tb00315.x**

Cockell, C.S., Gronstal, A.L., Voytek, M.A., Kirshtein, J.D., Finster, K., Sanford, W.E., Glamoclija, M., Gohn, G.S., Powars, D.S., and Wright Horton, J., Jr., 2009. Microbial abundance in the deep subsurface of the Chesapeake Bay impact crater: relationship to lithology and impact processes. *In* Gohn, G.S., Koeberl, C., Miller, K.G., and Reimold, W.U. (Eds.), *The ICDP-USGS Deep Drilling Project in the Chesapeake Bay Impact Structure: Results*

from the Eyreville Core Holes. Special Paper—Geological Society of America, 458:941–950. **http://dx.doi.org/10.1130/2009.2458(40)**

Cockell, C.S., Lee, P., Broady, P., Lim, D.S.S., Osinski, G.R., Parnell, J., Koeberl, C., Pesonen, L., and Salminen, J., 2005. Effects of asteroid and comet impacts on habitats for lithophytic organisms—a synthesis. *Meteoritics & Planetary Science,* 40(12):1901–1914. **http://dx.doi.org/10.1111/j.1945-5100.2005.tb00153.x**

Cockell, C.S., Lee, P., Osinski, G., Horneck, G., and Broady, P., 2002. Impact-induced microbial endolithic habitats. *Meteoritics & Planetary Science,* 37(10):1287–1298. **http://dx.doi.org/10.1111/j.1945-5100.2002.tb01029.x**

Collins, G.S., 2014. Numerical simulations of impact crater formation with dilatancy. *Journal of Geophysical Research: Planets,* 119(12):2600–2619. **http://dx.doi.org/10.1002/2014JE004708**

Collins, G.S., Melosh, H.J., Morgan, J.V., and Warner, M.R., 2002. Hydrocode simulations of Chicxulub crater collapse and peak-ring formation. *Icarus,* 157(1):24–33. **http://dx.doi.org/10.1006/icar.2002.6822**

Collins, G.S., Morgan, J., Barton, P., Christeson, G.L., Gulick, S., Urrutia, J., Warner, M., and Wünnemann, K., 2008. Dynamic modeling suggests terrace zone asymmetry in the Chicxulub crater is caused by target heterogeneity. *Earth and Planetary Science Letters,* 270(3–4):221–230. **http://dx.doi.org/10.1016/j.epsl.2008.03.032**

Coolen, M.J.L., Orsi, W.D., Balkema, C., Quince, C., Harris, K., Sylva, S.P., Filipova-Marinova, M., and Giosan, L., 2013. Evolution of the plankton paleome in the Black Sea from the Deglacial to Anthropocene. *Proceedings of the National Academy of Sciences of the United States of America,* 110(21):8609–8614. **http://dx.doi.org/10.1073/pnas.1219283110**

Coolen, M.J.L., and Overmann, J., 2007. 217 000-year-old DNA sequences of green sulfur bacteria in Mediterranean sapropels and their implications for the reconstruction of the paleoenvironment. *Environmental Microbiology,* 9(1):238–249. **http://dx.doi.org/10.1111/j.1462-2920.2006.01134.x**

Gelinas, A., Kring, D.A., Zurcher, L., Urrutia-Fucugauchi, J., Morton, O., and Walker, R.J., 2004. Osmium isotope constraints on the proportion of bolide component in Chicxulub impact melt rocks. *Meteoritics & Planetary Science,* 39(6):1003–1008. **http://dx.doi.org/10.1111/j.1945-5100.2004.tb00941.x**

Goderis, S., Paquay, F., and Claeys, P., 2012. Projectile identification in terrestrial impact structures and ejecta material. *In* Osinski, G.R., and Pierazzo, E. (Eds.), *Impact Cratering: Process and Products*: Oxford, United Kingdom (Blackwell Publishing, Ltd.), 223–235. **http://dx.doi.org/10.1002/9781118447307.ch15**

Goto, K., Tada, R., Tajika, E., Bralower, T.J., Hasegawa, T., and Matsui, T., 2004. Evidence for ocean water invasion into the Chicxulub crater at the Cretaceous/Tertiary boundary. *Meteoritics & Planetary Science,* 39(7):1233–1247. **http://dx.doi.org/10.1111/j.1945-5100.2004.tb01139.x**

Grieve, R.A.F., Langenhorst, F., and Stöffler, D., 1996. Shock metamorphism of quartz in nature and experiment: II. Significance in geoscience. *Meteoritics & Planetary Science,* 31(1):6–35. **http://dx.doi.org/10.1111/j.1945-5100.1996.tb02049.x**

Grieve, R.A.F., Reimold, W.U., Morgan, J., Riller, U., and Pilkington, M., 2008. Observations and interpretations at Vredefort, Sudbury, and Chicxulub: towards an empirical model of terrestrial impact basin formation. *Meteoritics & Planetary Science,* 43(5):855–882. **http://dx.doi.org/10.1111/j.1945-5100.2008.tb01086.x**

Gulick, S.P.S., Barton, P.J., Christeson, G.L., Morgan, J.V., McDonald, M., Mendoza-Cervantes, K., Pearson, Z.F., Surendra, A., Urrutia-Fucugauchi, J., Vermeesch, P.M., and Warner, M.R., 2008. Importance of pre-impact crustal structure for the asymmetry of the Chicxulub impact crater. *Nature Geoscience,* 1(2):131–135. **http://dx.doi.org/10.1038/ngeo103**

Gulick, S.P.S., Christeson, G.L., Barton, P.J., Grieve, R.A.F., Morgan, J.V., and Urrutia-Fucugauchi, J., 2013. Geophysical characterization of the Chicxulub impact crater. *Reviews of Geophysics,* 51(1):31–52. **http://dx.doi.org/10.1002/rog.20007**

Hecht, L., Wittmann, A., Schmitt, R.-T., and Stöffler, D., 2004. Composition of impact melt particles and the effects of post-impact alteration in suevitic rocks at the Yaxcopoil-1 drill core, Chicxulub crater, Mexico. *Meteoritics & Planetary Science,* 39(7):1169–1186. **http://dx.doi.org/10.1111/j.1945-5100.2004.tb01135.x**

Hildebrand, A.R., Penfield, G.T., Kring, D.A., Pilkington, M., Camargo, A.Z., Jacobsen, S.B., and Boynton, W.V., 1991. Chicxulub crater: a possible Cretaceous/Tertiary boundary impact crater on the Yucatán Peninsula, Mexico. *Geology,* 19(9):867–871. **http://dx.doi.org/10.1130/0091-7613(1991)019<0867:CCAPCT>2.3.CO;2**

Huber, M.S., Ferrière, L., Losiak, A., and Koeberl, C., 2011. ANIE: a mathematical algorithm for automated indexing of planar deformation features in quartz grains. *Meteoritics & Planetary Science,* 46(9):1418–1424. **http://dx.doi.org/10.1111/j.1945-5100.2011.01234.x**

Ivanov, B.A., 1994. Geomechanical models of impact cratering: Puchezh-Katunki structure. *In* Dressier, B.O., Grieve, R.A.F., and Sharpton, V.L. (Eds.), *Large Meteorite Impacts and Planetary Evolution.* Special Paper—Geological Society of America, 293:81–92. **http://dx.doi.org/10.1130/SPE293-p81**

Ivanov, B.A., 2005. Numerical modeling of the largest terrestrial meteorite craters. *Solar System Research,* 39(5):381–409. **http://dx.doi.org/10.1007/s11208-005-0051-0**

Jiang, S., Bralower, T.J., Patzkowsky, M.E., Kump, L.R., and Schueth, J.D., 2010. Geographic controls on nannoplankton extinction across the Cretaceous/Palaeogene boundary. *Nature Geoscience,* 3(4):280–285. **http://dx.doi.org/10.1038/ngeo775**

John, C.M., Banerjee, N.R., Longstaffe, F.J., Sica, C., Law, K.R., and Zachos, J.C., 2012. Clay assemblage and oxygen isotopic constraints on the weathering response to the Paleocene-Eocene Thermal Maximum, east coast of North America. *Geology,* 40(7):591–594. **http://dx.doi.org/10.1130/G32785.1**

Kenkmann, T., 2003. Dike formation, cataclastic flow, and rock fluidization during impact cratering: an example from the Upheaval Dome structure, Utah. *Earth and Planetary Science Letters,* 214(1–2):43–58. **http://dx.doi.org/10.1016/S0012-821X(03)00359-5**

Kenkmann, T., Jahn, A., Scherler, D., and Ivanov, B.A., 2005. Structure and formation of a central uplift: a case study at the Upheaval Dome impact crater, Utah. *In* Kenkmann, T., Hörz, F., and Deutsch, A. (Eds.), *Large Meteorite Impacts III.* Special Paper—Geological Society of America, 384:85–115. **http://dx.doi.org/10.1130/0-8137-2384-1.85**

Kenkmann, T., Wittmann, A., and Scherler, D., 2004. Structure and impact indicators of the Cretaceous sequence of the ICDP drill core Yaxcopoil-1, Chicxulub impact crater, Mexico. *Meteoritics & Planetary Science,* 39(7):1069–1088. **http://dx.doi.org/10.1111/j.1945-5100.2004.tb01129.x**

Kettrup, B., Deutsch, A., Ostermann, M., and Agrinier, P., 2000. Chicxulub impactites: geochemical clues to the precursor rocks. *Meteoritics & Planetary Science,* 35(6):1229–1238. **http://dx.doi.org/10.1111/j.1945-5100.2000.tb01511.x**

Koeberl, C., Claeys, P., Hecht, L., and McDonald, I., 2012. Geochemistry of impactites. *Elements,* 8(1):37–42. **http://dx.doi.org/10.2113/gselements.8.1.37**

Kring, D.A., 2005. Hypervelocity collisions into continental crust composed of sediments and an underlying crystalline basement: comparing the Ries (~24 km) and Chicxulub (~180 km) impact craters. *Chemie der Erde–Geochemistry,* 65(1):1–46. **http://dx.doi.org/10.1016/j.chemer.2004.10.003**

Kring, D.A., and Cohen, B.A., 2002. Cataclysmic bombardment throughout the inner solar system 3.9–4.0 Ga. *Journal of Geophysical Research: Planets,* 107(E2):1–6. **http://dx.doi.org/10.1029/2001JE001529**

Kring, D.A., Hörz, F., Zurcher, L., and Urrutia Fucugauchi, J., 2004. Impact lithologies and their emplacement in the Chicxulub impact crater: initial results from the Chicxulub Scientific Drilling Project, Yaxcopoil, Mexico. *Meteoritics & Planetary Science,* 39(6):879–897. **http://dx.doi.org/10.1111/j.1945-5100.2004.tb00936.x**

Lieger, D., Riller, U., and Gibson, R.L., 2009. Generation of fragment-rich pseudotachylite bodies during central uplift formation in the Vredefort

impact structure, South Africa. *Earth and Planetary Science Letters,* 279(1–2):53–64. **http://dx.doi.org/10.1016/j.epsl.2008.12.031**

Lüders, V., and Rickers, K., 2004. Fluid inclusion evidence for impact-related hydrothermal fluid and hydrocarbon migration in Cretaceous sediments of the ICDP-Chicxulub drill core Yaxcopoil-1. *Meteoritics & Planetary Science,* 39(7):1187–1197. **http://dx.doi.org/10.1111/j.1945-5100.2004.tb01136.x**

Melosh, H.J., 1979. Acoustic fluidization: a new geologic process? *Journal of Geophysical Research: Solid Earth,* 84(B13):7513–7520. **http://dx.doi.org/10.1029/JB084iB13p07513**

Melosh, H.J., and Ivanov, B.A., 1999. Impact crater collapse. *Annual Review of Earth and Planetary Sciences,* 27(1):385–415. **http://dx.doi.org/10.1146/annurev.earth.27.1.385**

Mohr-Westheide, T., Reimold, W.U., Riller, U., and Gibson, R.L., 2009. Pseudotachylitic breccia and microfracture networks in Archean gneiss of the central uplift of the Vredefort Impact Structure, South Africa. *South African Journal of Geology,* 112(1):1–22. **http://dx.doi.org/10.2113/gssajg.112.1.1**

Morgan, J., and Warner, M., 1999. Chicxulub: the third dimension of a multi-ring impact basin. *Geology,* 27(5):407–410. **http://dx.doi.org/10.1130/0091-7613(1999)027<0407:CTTDOA>2.3.CO;2**

Morgan, J., Warner, M., the Chicxulub Working Group, Brittan, J., Buffler, R., Carmargo, A., Christeson, G., Denton, P., Hildebrand, A., Hobbs, R., Macintyre, H., Mackenzie, G., Maguire, P., Marin, L., Nakamura, Y., Pilkington, M., Sharpton, V., Snyder, D., Suarez, G., and Trejo, A., 1997. Size and morphology of the Chicxulub impact crater. *Nature,* 390(6659):472–476. **http://dx.doi.org/10.1038/37291**

Morgan, J.V., Warner, M.R., Collins, G.S., Grieve, R.A.F., Christeson, G.L., Gulick, S.P.S., and Barton, P.J., 2011. Full waveform tomographic images of the peak ring at the Chicxulub impact crater. *Journal of Geophysical Research: Solid Earth,* 116(B6):B06303. **http://dx.doi.org/10.1029/2010JB008015**

Morgan, J.V., Warner, M.R., Collins, G.S., Melosh, H.J., and Christeson, G.L., 2000. Peak-ring formation in large impact craters: geophysical constraints from Chicxulub. *Earth and Planetary Science Letters,* 183(3–4):347–354. **http://dx.doi.org/10.1016/S0012-821X(00)00307-1**

O'Keefe, J.D., and Ahrens, T.J., 1993. Planetary cratering mechanics. *Journal of Geophysical Research: Planets*, 98(E9):17011–17028. **http://dx.doi.org/10.1029/93JE01330**

Osinski, G.R., Lee, P., Parnell, J., Spray, J.G., and Baron, M., 2005. A case study of impact-induced hydrothermal activity: the Haughton impact structure, Devon Island, Canadian High Arctic. *Meteoritics & Planetary Science,* 40(12):1859–1877. **http://dx.doi.org/10.1111/j.1945-5100.2005.tb00150.x**

Osinski, G.R., Tornabene, L.L., Banerjee, N.R., Cockell, C.S., Flemming, R., Izawa, M.R.M., McCutcheon, J., Parnell, J., Preston, L.J., Pickersgill, A.E., Pontefract, A., Sapers, H.M., and Southam, G., 2013. Impact-generated hydrothermal systems on Earth and Mars. *Icarus,* 224(2):347–363. **http://dx.doi.org/10.1016/j.icarus.2012.08.030**

Pickersgill, A.E., Osinksi, G.R., and Flemming, R.L., 2015. Shock effects in plagioclase feldspar from the Mistastin Lake impact structure, Canada. *Meteoritics & Planetary Science,* 50(9):1546–1561. **http://dx.doi.org/10.1111/maps.12495**

Pierazzo, E., Hahmann, A.N., and Sloan, L.C., 2003. Chicxulub and climate: radioactive perturbations of impact-produced S-bearing gases. *Astrobiology,* 3(1):99–118. **http://dx.doi.org/10.1089/153110703321632453**

Pope, K.O., Baines, K.H., Ocampo, A.C., and Ivanov, B.A., 1997. Energy, volatile production, and climatic effects of the Chicxulub Cretaceous/Tertiary impact. *Journal of Geophysical Research: Planets*, 102(E9):21645–21664. **http://dx.doi.org/10.1029/97JE01743**

Quesnel, Y., Gattacceca, J., Osinski, G.R., and Rochette, P., 2013. Origin of the central magnetic anomaly at the Haughton impact structure, Canada. *Earth and Planetary Science Letters,* 367:116–122. **http://dx.doi.org/10.1016/j.epsl.2013.02.032**

Rae, A.S.P., Morgan, J.V., Collins, G.S., Osinski, G.R., and Grieve, R.A.F., 2015. Observational constraints on structural uplift formation: the West Clearwater impact structure [presented at 46th Lunar and Planetary Science Conference, The Woodlands, Texas, 16–20 March 2015]. (Abstract 1451) **http://www.hou.usra.edu/meetings/lpsc2015/pdf/1451.pdf**

Rebolledo-Vieyra, M., and Urrutia-Fucugauchi, J., 2004. Magnetostratigraphy of the impact breccias and post-impact carbonates from borehole Yaxcopoil-1, Chicxulub impact crater, Yucatán, Mexico. *Meteoritics & Planetary Science,* 39(6):821–830. **http://dx.doi.org/10.1111/j.1945-5100.2004.tb00932.x**

Rebolledo-Vieyra, M., and Urrutia-Fucugauchi, J., 2006. Magnetostratigraphy of the Cretaceous/Tertiary boundary and early Paleocene sedimentary sequence from the Chicxulub impact crater. *Earth, Planets and Space,* 58(10):1309–1314. **http://dx.doi.org/10.1186/BF03352626**

Reimold, W.U., and Gibson, R.L., 2005. "Pseudotachylites" in large impact structures. *In* Koeberl, C., and Henkel, H. (Eds.), *Impact Studies* (Volume 6): *Impact Tectonics.* Koeberl, C. (Series Ed.): New York (Springer-Verlag), 1–53. **http://dx.doi.org/10.1007/3-540-27548-7_1**

Renne, P.R., Deino, A.L., Hilgen, F.J., Kuiper, K.F., Mark, D.F., Mitchell, W.S., III, Morgan, L.E., Mundil, R., and Smit, J., 2013. Time scales of critical events around the Cretaceous-Paleogene boundary. *Science,* 339(6120):684–687. **http://dx.doi.org/10.1126/science.1230492**

Riller, U., and Lieger, D., 2008. Geological evidence for acoustic fluidization in large impact structures [presented at Large Meteorites and Planetary Evolution IV, Vredefort Dome, South Africa, 17–21 August 2008]. (Abstract 3025) **http://www.lpi.usra.edu/meetings/lmi2008/pdf/3025.pdf**

Riller, U., Lieger, D., Gibson, R.L. Grieve, R.A.F., and Stöffler, D., 2010. Origin of large-volume pseudotachylite in terrestrial impact structures. *Geology,* 38(7):619–622. **http://dx.doi.org/10.1130/G30806.1**

Rowe, A.J., Wilkinson, J.J, Coles, B.J., and Morgan, J.V., 2004. Chicxulub: testing for post-impact hydrothermal inputs into the Tertiary ocean. *Meteoritics & Planetary Science,* 39(7):1223–1231. **http://dx.doi.org/10.1111/j.1945-5100.2004.tb01138.x**

Sanford, J.C., Snedden, J.W., and Gulick, S.P.S., in press. The Cretaceous-Paleogene boundary deposit in the Gulf of Mexico: large-scale oceanic basin response to the Chicxulub impact. *Journal of Geophysical Research: Solid Earth.* **http://dx.doi.org/10.1002/2015JB012615**

Sato, H., Onoue, T., Nozaki, T., and Suzuki, K., 2013. Osmium isotope evidence for a large late Triassic impact event. *Nature Communications,* 4:2455. **http://dx.doi.org/10.1038/ncomms3455**

Sato, H., Shirai, N., Ebihara, M., Onoue, T., and Kiyokawa, S., 2016. Sedimentary PGE signatures in the late Triassic ejecta deposits from Japan: implications for the identification of impactor. *Palaeogeography, Palaeoclimatology, Palaeoecology,* 442:36–47. **http://dx.doi.org/10.1016/j.palaeo.2015.11.015**

Schulte, P., Alegret, L., Arenillas, I., Arz, J.A., Barton, P.J., Bown, P.R., Bralower, T.J., Christeson, G.L., Claeys, P., Cockell, C.S., Collins, G.S., Deutsch, A., Goldin, T.J., Goto, K., Grajales-Nishimura, J.M., Grieve, R.A.F., Gulick, S.P.S., Johnson, K.R., Kiessling, W., Koeberl, C., Kring, D.A., MacLeod, K.G., Matsui, T., Melosh, J., Montanari, A., Morgan, J.V., Neal, C.R., Nichols, D.J., Norris, R.D., Pierazzo, E., Ravizza, G., Rebolledo-Vieyra, M., Reimold, W.U., Robin, E., Salge, T., Speijer, R.P., Sweet, A.R., Urrutia-Fucugauchi, J., Vajda, V., Whalen, M.T., and Willumsen, P.S., 2010. The Chicxulub asteroid impact and mass extinction at the Cretaceous–Paleogene boundary. *Science,* 327:1214–1218. **http://dx.doi.org/10.1126/science.1177265**

Schwenzer, S.P., and Kring, D.A., 2009. Impact-generated hydrothermal systems capable of forming phyllosilicates on Noachian Mars. *Geology,* 37(12):1091–1094. **http://dx.doi.org/10.1130/G30340A.1**

Senft, L.E., and Stewart, S.T., 2009. Dynamic fault weakening and the formation of large impact craters. *Earth and Planetary Science Letters,* 287(3–4):471–482. **http://dx.doi.org/10.1016/j.epsl.2009.08.033**

Sharpton, V.L., Marin, L.E., Carney, J.L., Lee, S., Ryder, G., Schuraytz, B.C., Sikora, P., and Spudis, P.D., 1996. A model of the Chicxulub impact basin based on evaluation of geophysical data, well logs, and drill core samples. *In* Ryder, G., Fastovsky, D.E, and Gartner, S. (Eds.), *The Cretaceous-Tertiary Event and Other Catastrophes in Earth History.* Special Paper—

Geological Society of America, 307:55–74. **http://dx.doi.org/10.1130/0-8137-2307-8.55**

Smit, J., Van Der Gaast, S., and Lustenhouwer, W., 2004. Is the transition impact to post-impact rock complete? Some remarks based on XRF scanning, electron microprobe, and thin section analyses of the Yaxcopoil-1 core in the Chicxulub crater. *Meteoritics & Planetary Science,* 39(7):1113–1126. **http://dx.doi.org/10.1111/j.1945-5100.2004.tb01132.x**

Spray, J.G., 1992. A physical basis for the frictional melting of some rock-forming minerals. *Tectonophysics,* 204(3–4):205–221. **http://dx.doi.org/10.1016/0040-1951(92)90308-S**

Stöffler, D., Artemieva, N.A., Ivanov, B.A., Hecht, L., Kenkmann, T., Schmitt, R.T., Tagle, R.A., and Wittmann, A., 2004. Origin and emplacement of the impact formations at Chicxulub, Mexico, as revealed by the ICDP deep drilling at Yaxcopoil-1 and by numerical modeling. *Meteoritics & Planetary Science,* 39(7):1035–1067. **http://dx.doi.org/10.1111/j.1945-5100.2004.tb01128.x**

Tagle, R., and Hecht, L., 2006. Geochemical identification of projectiles in impact rocks. *Meteoritics & Planetary Science,* 41(11):1721–1735. **http://dx.doi.org/10.1111/j.1945-5100.2006.tb00448.x**

Tikoo, S.M., Gattacceca, J., Swanson-Hysell, N.L., Weiss, B.P., Suavet, C., and Cournède, C., 2015. Preservation and detectability of shock-induced magnetization. *Journal of Geophysical Research: Planets,* 120(9):1461–1475. **http://dx.doi.org/10.1002/2015JE004840**

Tomioka, N., Tomeoka, K., Nakamura-Messenger, K., and Sekine, T., 2007. Heating effects of the matrix of experimentally shocked Murchison CM chondrite: comparison with micrometeorites. *Meteoritics & Planetary Science,* 42(1):19–30. **http://dx.doi.org/10.1111/j.1945-5100.2007.tb00214.x**

Trinquier, A., Birck, J.-L., and Allègre, C.J., 2006. The nature of the KT impactor. A ^{54}Cr reappraisal. *Earth and Planetary Science Letters,* 241(3–4):780–788. **http://dx.doi.org/10.1016/j.epsl.2005.11.006**

Urrutia-Fucugauchi, J., Camargo-Zanoguera, A., Pérez-Cruz, L., and Pérez-Cruz, G., 2011. The Chicxulub multi-ring impact crater, Yucatán carbonate platform, Gulf of Mexico. *Geofísica Internacional,* 50(1):99–127. **http://www.scielo.org.mx/pdf/geoint/v50n1/v50n1a9.pdf**

Urrutia-Fucugauchi, J., Chavez-Aguirre, J.M., Pérez-Cruz, L., and De La Rosa, J.L., 2008. Impact ejecta and carbonate sequence in the eastern sector of the Chicxulub crater. *Comptes Rendus Geoscience,* 341(12):801–810. **http://dx.doi.org/10.1016/j.crte.2008.09.001**

Urrutia-Fucugauchi, J., Marin, L., and Trejo-Garcia, A., 1996. UNAM scientific drilling program of Chicxulub impact structure—evidence for a 300 kilometer crater diameter. *Geophysical Research Letters,* 23(13):1565–1568. **http://dx.doi.org/10.1029/96GL01566**

Urrutia-Fucugauchi, J., Morgan, J., Stöffler, D., and Claeys, P., 2004. The Chicxulub Scientific Drilling Project (CSDP). *Meteoritics & Planetary Science,* 39(6):787–790. **http://dx.doi.org/10.1111/j.1945-5100.2004.tb00928.x**

Vellekoop, J., Sluijs, A., Smit, J., Schouten, S., Weijers, J.W.H., Sinninghe Damsté, J.S., and Brinkhuis, H., 2014. Rapid short-term cooling following the Chicxulub impact at the Cretaceous-Paleogene boundary. *Proceedings of the National Academy of Sciences of the United States of America,* 111(21):7537–7541. **http://dx.doi.org/10.1073/pnas.1319253111**

Vermeesch, P.M., and Morgan, J.V., 2008. Structural uplift beneath the Chicxulub impact structure. *Journal of Geophysical Research: Solid Earth,* 113(B7):B07103. **http://dx.doi.org/10.1029/2007JB005393**

Ward, W.C., Keller, G., Stinnesbeck, W., and Adatte, T., 1995. Yucatán subsurface stratigraphy: implications and constraints for the Chicxulub impact. *Geology,* 23(10):873–876. **http://dx.doi.org/10.1130/0091-7613(1995)023<0873:YNSSIA>2.3.CO;2**

Whalen, M.T., Gulick, S.P.S., Pearson, Z.F., Norris, R.D., Perez Cruz, L., and Urrutia Fucugauchi, J., 2013. Annealing the Chicxulub impact: Paleogene Yucatàn carbonate slope development in the Chicxulub impact basin, Mexico. *In* Verwer, K., Playton, T.E., and Harris, P.M. (Eds.), *Deposits, Architecture, and Controls of Carbonate Margin, Slope and Basinal Settings.* Special Publication - SEPM (Society for Sedimentary Geology), 105:282–304. **http://dx.doi.org/10.2110/sepmsp.105.04**

Whalen, M.T., Pearson, Z.F., Gulick, S.P.S., and Norris, R.D., 2008. Sequence stratigraphy of the Chicxulub crater infill and Yucatán carbonate platform development: implications for the evolution of large terrestrial impact craters. *Geological Society of America Abstracts with Programs,* 40(6):407. **https://gsa.confex.com/gsa/2008AM/finalprogram/abstract_151599.htm**

Wittmann, A., Kenkmann, T., Hecht, L., and Stöffler, D., 2007. Reconstruction of the Chicxulub ejecta plume from its deposits in drill core Yaxcopoil-1. *Geological Society of America Bulletin,* 119(9–10):1151–1167. **http://dx.doi.org/10.1130/B26116.1**

Wittmann, A., Kenkmann, T., Schmitt, R.T., Hecht, L., and Stöffler, D., 2004. Impact-related dike breccia lithologies in the ICDP drill core Yaxcopoil-1, Chicxulub impact structure, Mexico. *Meteoritics & Planetary Science,* 39(6):931–954. **http://dx.doi.org/10.1111/j.1945-5100.2004.tb00938.x**

Wittmann, A., Schmitt, R.T., Hecht, L., Kring, D.A., Reimold, W.U., and Povenmire, H., 2009. Petrology of impact melt rocks from the Chesapeake Bay crater, USA. *Special Paper - Geological Association of America,* 458:377–396. **http://dx.doi.org/10.1130/2009.2458(17)**

Wünnemann, K., Morgan, J.V., and Jödicke, H., 2005. Is Ries crater typical for its size? An analysis based upon old and new geophysical data and numerical modeling. *In* Kenkmann, T., Hörz, F., and Deutsch, A. (Eds.), *Large Meteorite Impacts III.* Special Paper—Geological Society of America, 384:67–83. **http://dx.doi.org/10.1130/0-8137-2384-1.67**

Yamaguchi, K.E., Johnson, C.M., Beard, B.L., and Ohmoto, H., 2005. Biogeochemical cycling of iron in the Archean–Paleoproterozoic Earth: constraints from iron isotope variations in sedimentary rocks from the Kaapvaal and Pilbara Cratons. *Chemical Geology,* 218(1–2):135–169. **http://dx.doi.org/10.1016/j.chemgeo.2005.01.020**

Zürcher, L., and Kring, D.A., 2004. Hydrothermal alteration in the core of the Yaxcopoil-1 borehole, Chicxulub impact structure, Mexico. *Meteoritics & Planetary Science,* 39(7):1199–1221. **http://dx.doi.org/10.1111/j.1945-5100.2004.tb01137.x**

Zachos, J., Pagani, M., Sloan, L., Thomas, E., and Billups, K., 2001. Trends, rhythms, and aberrations in global climate 65 Ma to present. *Science,* 292(5517):686–693. **http://dx.doi.org/10.1126/science.1059412**

Table T1. Hole M0077A summary. Note that percent recovery exceeds 100% due to differences between drilling depth below seafloor (DSF) and the measured length of core recovered.

Hole	Location	Water depth (m)	Cores (*N*)	Interval cored DSF (m)	Interval open holed DSF (m)	Penetration depth DSF (m)	Core recovered (m)	Core recovery (%)
M0077A	21 27.009′N, 89 56.962′W	19.80 m	303	828.99	505.7	1334.69	839.51	101.27

Table T2. Lithostratigraphic units, Hole M0077A. Determined using Corelyzer. Boundary is defined at the average depth if it is inclined. Bottom of Unit 3B is defined as first occurrence of granitic rocks.

Unit	Top depth (mbsf)	Bottom depth (mbsf)	Top core, section, interval (cm)	Bottom core, section, interval (cm)	Thickness (m)	Top boundary definition
1A	505.70	530.18	1R-1, 0	1R-2, 116.8	24.48	Top of core
1B	530.18	537.80	11R-2, 116.8	14R-1, 86.40	7.62	Sharp erosional contact that truncates underlying thin grainstone
1C	537.80	559.75	14R-1, 86.40	21R-1, 146.20	21.95	Erosional contact that truncates underlying dark marlstone/claystone
1D	559.75	580.89	21R-1, 146.20	28R-1, 125.20	21.14	Gradational contact designated as the last dark millimeter-scale marlstone/limestone
1E	580.89	607.27	28R-1, 125.20	37R-1, 25.60	26.38	Change to bluish colored marlstones at the top
1F	607.27	616.58	37R-1, 25.60	40R-1, 34.20	9.31	Top of a prominent carbonate cemented surface
1G	616.58	617.33	40R-1, 34.20	40R-1, 109.4	0.75	Contact between light green claystone and underlying brown siltstone
2A	617.33	664.52	40R-1, 109.4	55R-3, 11	47.19	Sharp stylolitized contact at top of suevite
2B	664.52	712.84	55R-3, 11	83R-1, 75	48.32	Erosional contact at Section 55R-3, 6–16 cm
2C	712.84	721.61	83R-1, 75	87R-2, 90	8.77	Gradational change from mid-brown suevite matrix with subangular to subrounded clasts to dark-brown suevite matrix with angular to subangular clasts
3A	721.61	737.56	87R-2, 90	92R-3, 17	15.95	First occurrence of massive black melt rock with green schlieren
3B	737.56	747.02	92R-3, 17	95R-3, 117	9.46	Last occurrence of massive black melt rock with green schlieren
4	747.02	1334.73	95R-3, 117	303R-3, 51	587.67	First occurrence of granitoid larger than 1 m

Figure F1. Peak rings are roughly circular rings of rugged hills and massifs that stand above the otherwise flat crater floor. In peak-ring basins, the crater rim is the outer edge of a terrace zone. In multi-ring basins, two or more rings (inward-facing asymmetric scarps) lie outboard of the central basin. Photo credit: NASA.

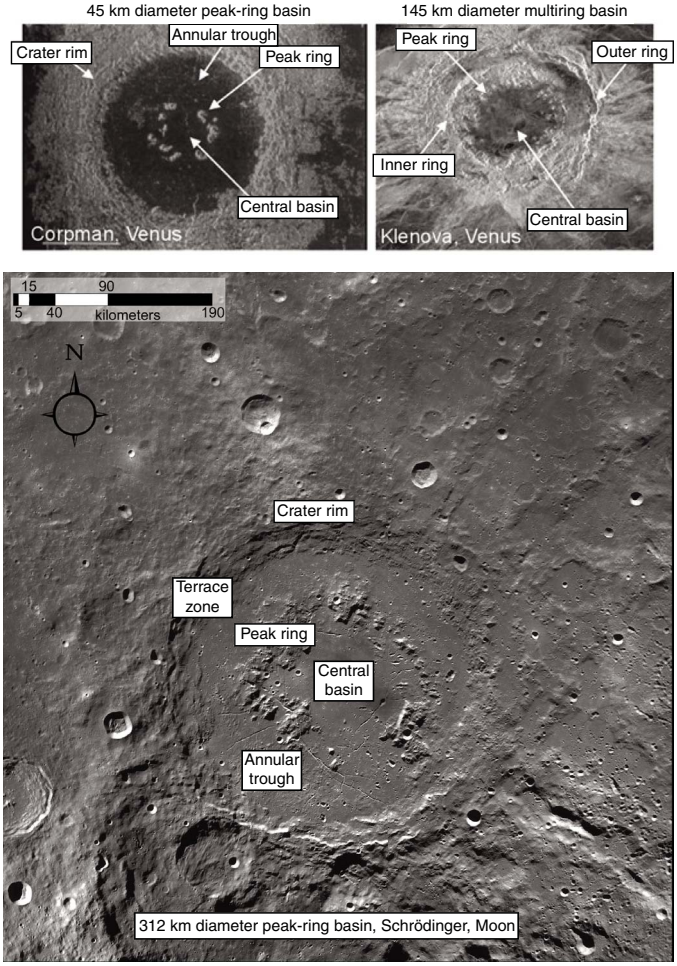

Figure F2. Location of site survey data overlain on the gravity field. Coastline is in white. Small black dots are cenotés. Marine seismic profiles acquired in 1996 and 2005 are shown in black dashed and solid lines, respectively. Offshore and onshore seismometer locations in the 1996 and 2005 surveys are shown with large black and white circles, respectively. Existing well locations are shown with yellow squares. Proposed Sites Chicx-03A and Chicx-04A are shown with yellow triangles. Expedition 364 drilled Hole M0077A (proposed Site Chicx-03B), located 250 m southeast of Site Chicx-03A, to 1500 m DSF. Modified from Gulick et al. (2013); from American Geophysical Union.

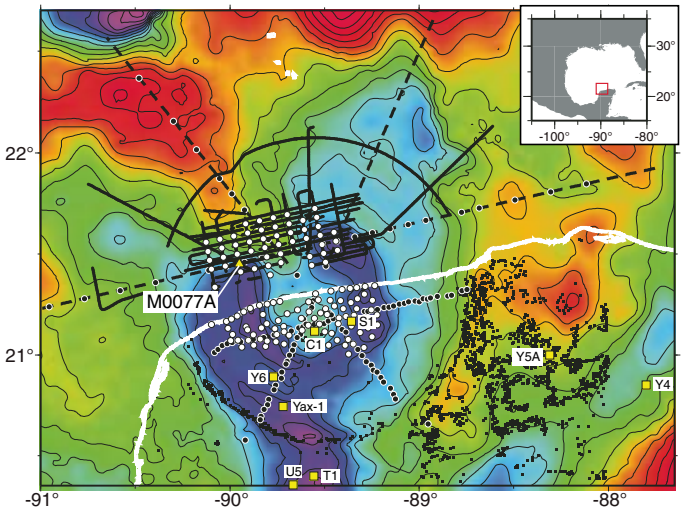

Figure F3. Seismic reflection data along Chicx-A. At about 20–30 km outboard of the crater rim at Chicxulub, the relatively undisturbed, flat-lying, pre-impact stratigraphy is abruptly offset vertically by 400–500 m (outer ring). The outer ring faults are observed out to radial distances of 90–120 km, giving a crater diameter of ~195–210 km (Morgan et al., 1997; Gulick et al., 2008). Modified from Gulick et al. (2008); from *Nature Geoscience*.

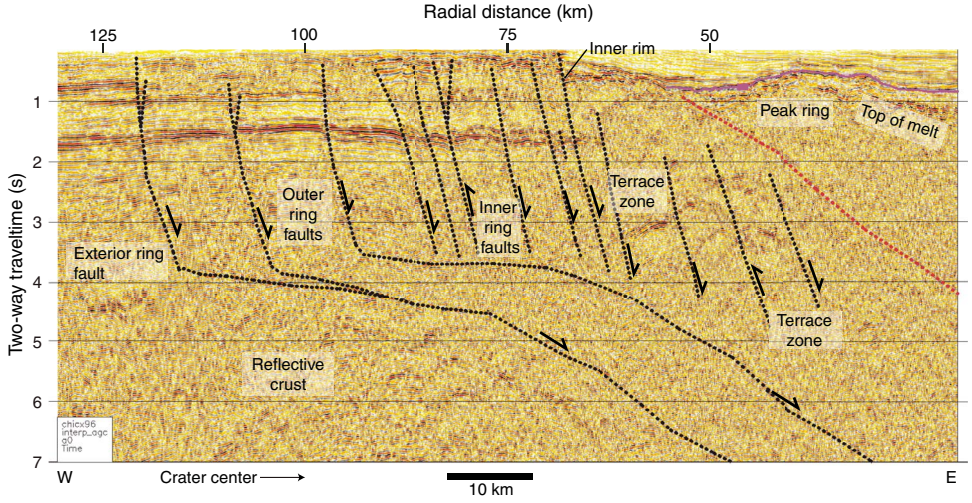

Figure F4. Hole M0077A projected onto a seismic reflection profile and velocity model obtained from full-waveform inversion. Core was recovered between 505.7 and 1334.73 mbsf. The principal targets were the PETM at ~600 mbsf, followed by the K-Pg boundary at ~650 mbsf and the rocks that form the peak ring. The uppermost peak-ring rocks are formed from 100–150 m of low-velocity material, below which there is a low-frequency reflector coincident with an increase in velocity. Modified from Morgan et al. (2011); from American Geophysical Union.

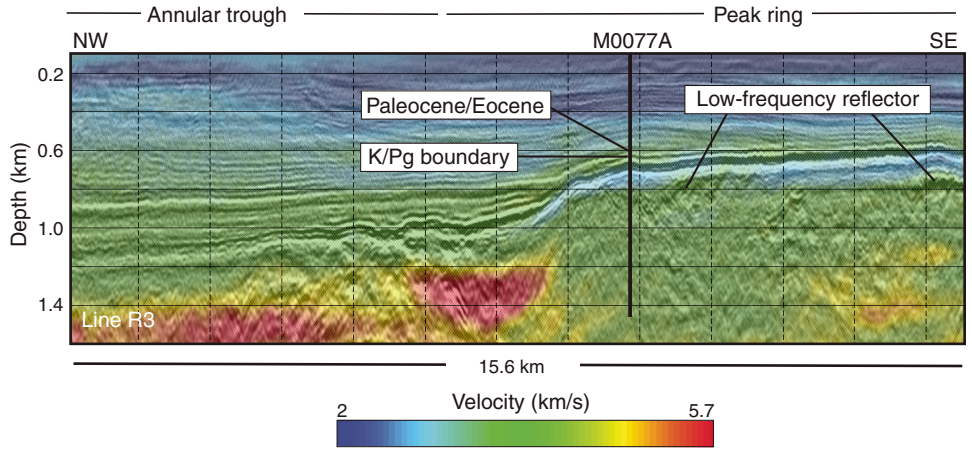

Figure F5. Hydrocode simulation of the formation of the Chicxulub crater (Collins et al., 2002; Morgan et al., 2011). Layering shows stratigraphy; impact point and center of crater are at a horizontal distance of 0 km. (A) Sediments that form the transient cavity rim collapsed inward and downward, whereas (B) material in the central crater collapsed upward. C. In this model, the stratigraphically uplifted material (central uplift) collapses outward across the downthrown rim material to form a peak ring. D. Cross section through the final crater. Color shows maximum shock pressures to which rocks have been subjected during crater formation. Dashed line = location of sediments that originally formed the transient cavity rim (see A). Modified from Morgan et al. (2011); from American Geophysical Union.

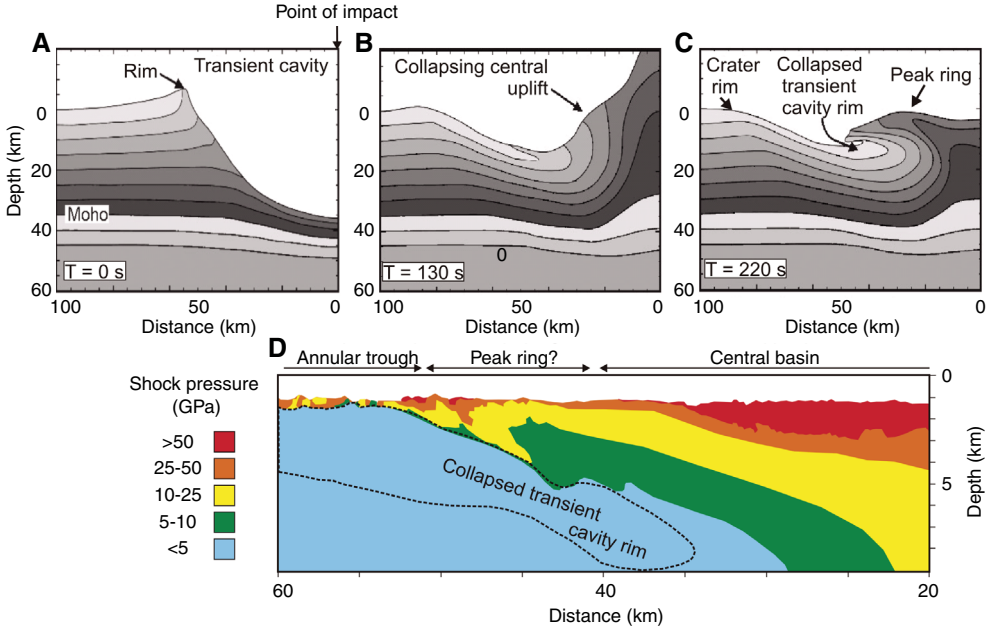

Figure F6. A. Location map showing onshore drill holes from the UNAM scientific drilling program (Holes U1–U8), the ICDP borehole (Yax-1), and PeMex drilling. All parts modified from Rebolledo-Vieyra and Urrutia-Fucugauchi (2004); from The Meteorological Society. (Continued on next two pages.)

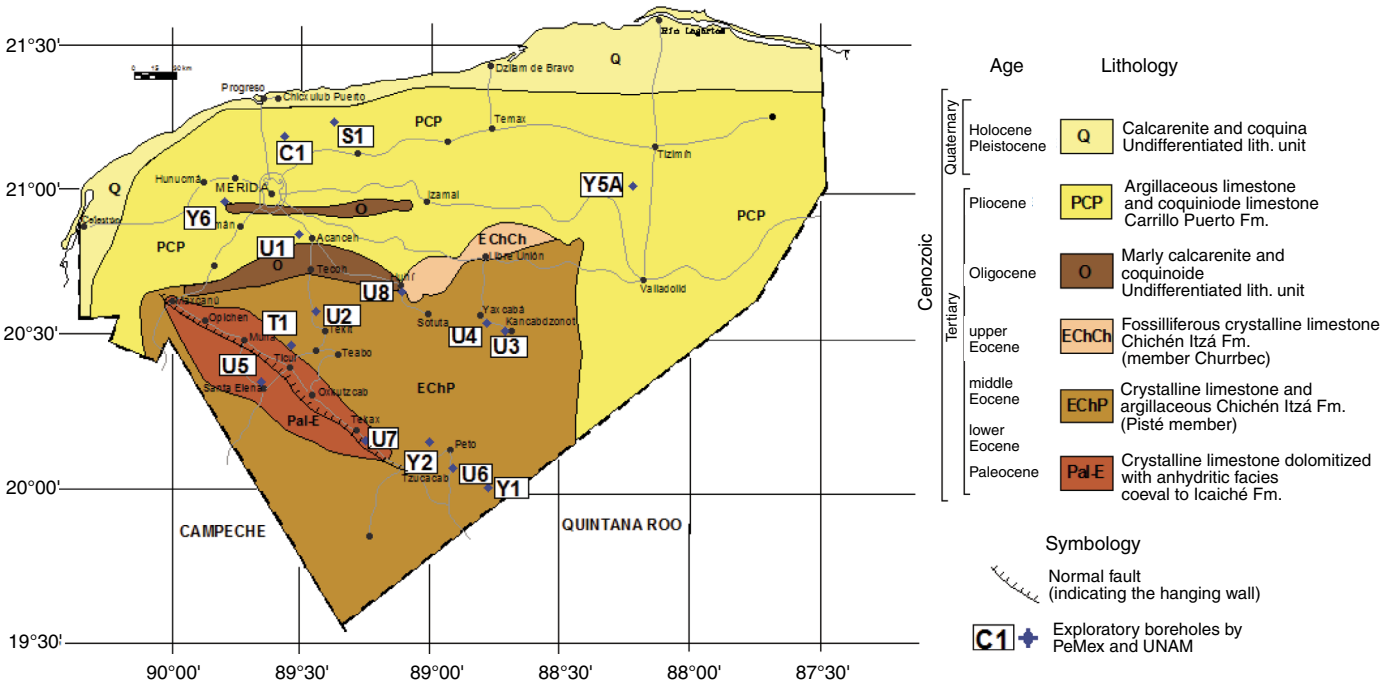

Figure F6 (continued). B. Lithologic columns and stratigraphy from PeMex and Yax-1 boreholes. Site M0077 is ~45 km from the crater center. (Continued on next page.)

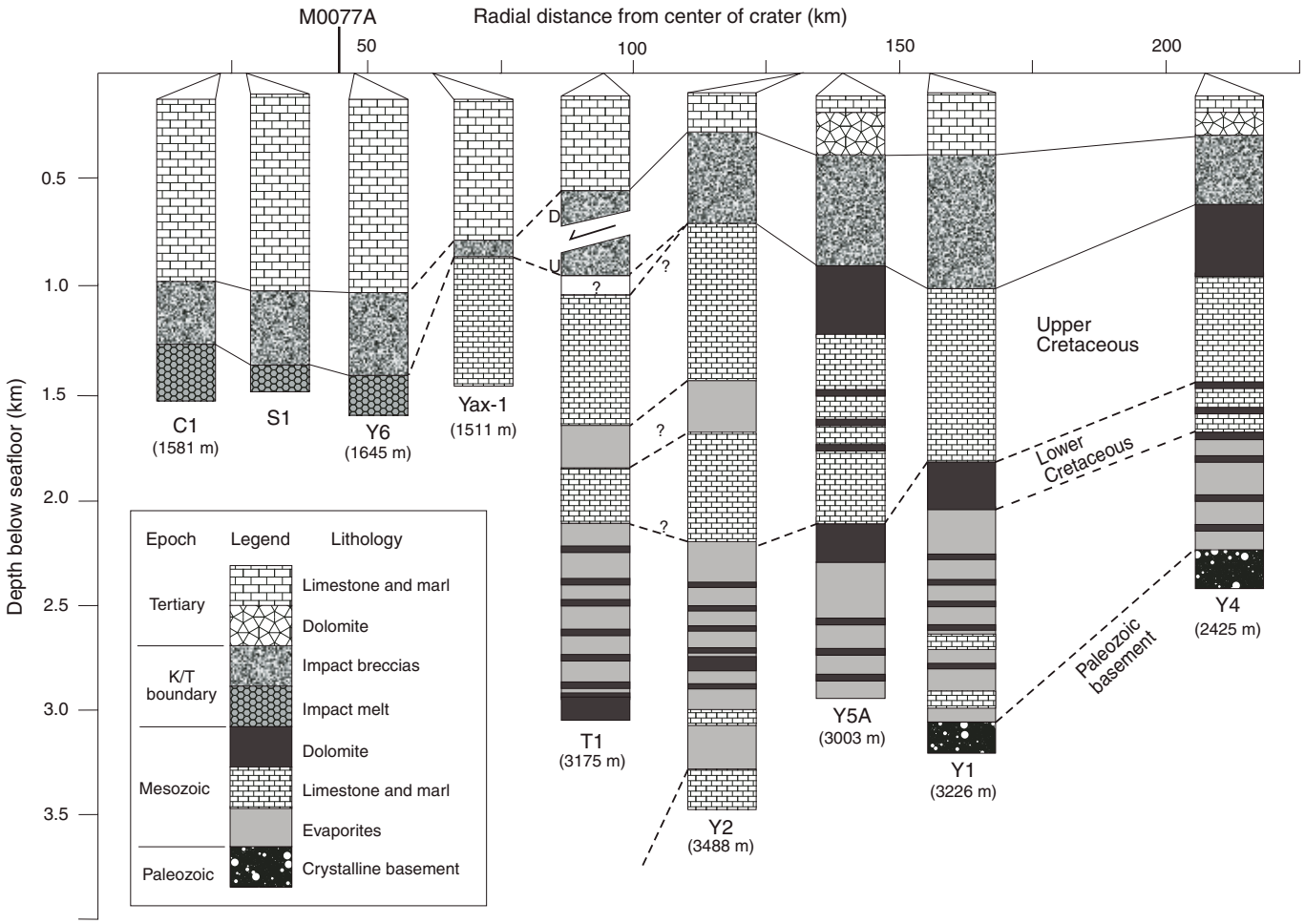

Figure F6 (continued). C. Lithologic columns and stratigraphy from UNAM and Yax-1 boreholes.

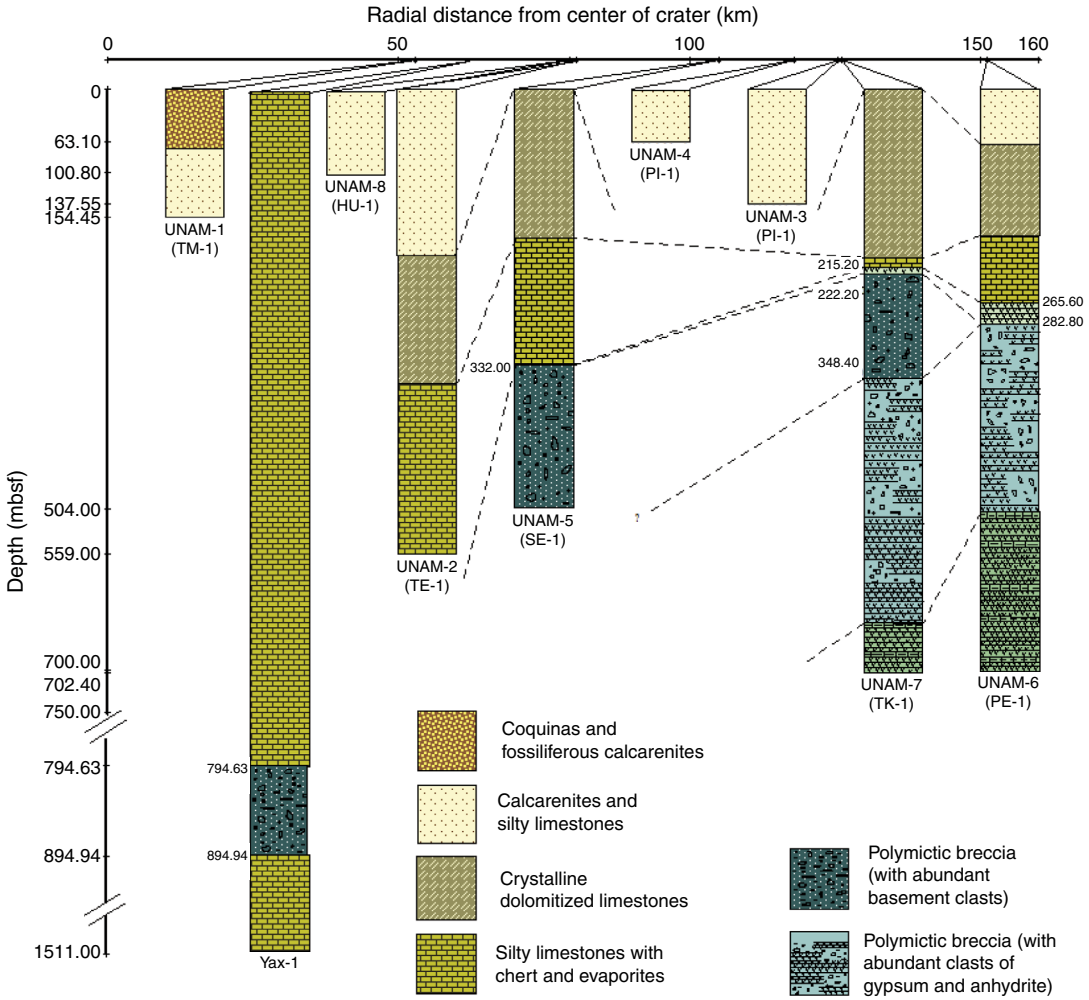

Figure F7. Numerical modeling of a hydrothermal system through a peak ring in a large impact structure (redrawn from Abramov and Kring, 2007).

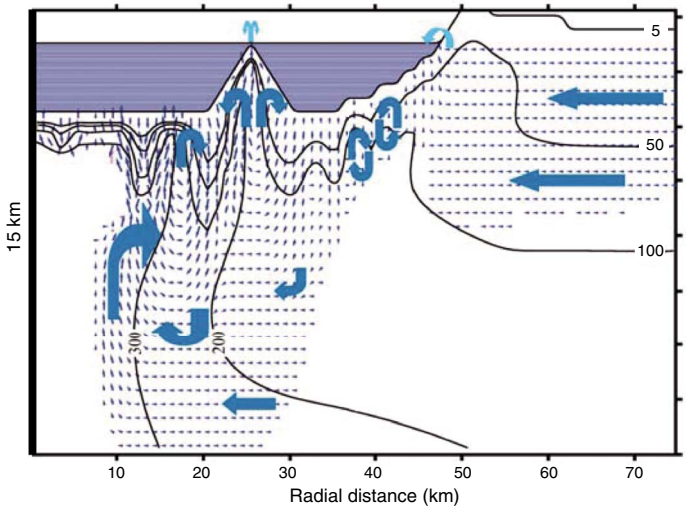

Figure F8. Microbial enumerations (log abundance per gram dry weight) through the Chesapeake Bay impact structure, showing a modern-day microbial habitat in the impactites. Modified from Cockell et al. (2009); from *Geological Society of America Special Papers*.

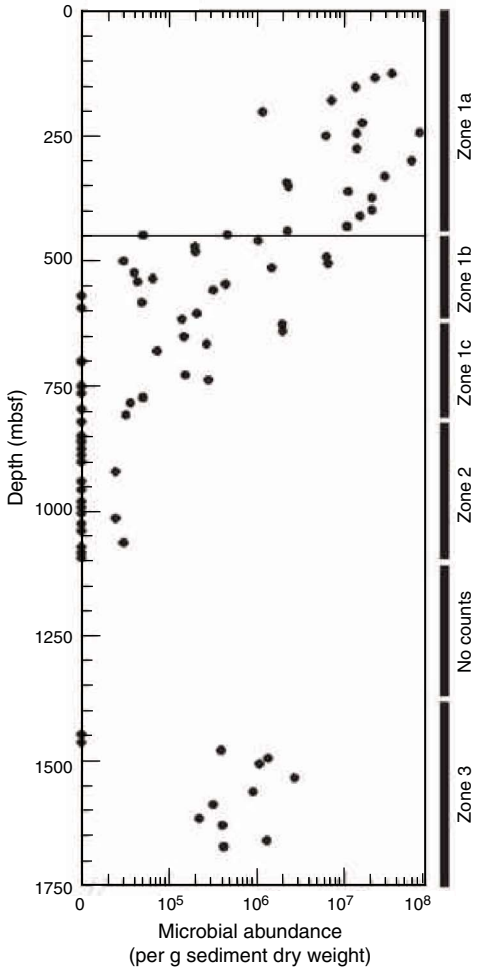

Figure F9. Generalized climate curve for the Cretaceous and Paleogene derived from deep-sea benthic oxygen isotope data (Zachos et al., 1993, 2001). Also shown: Eocene/Oligocene boundary, PETM, late Paleocene biotic event (LPTM), Cretaceous/Paleogene (K-Pg) boundary, mid-Maastrichtian event (MME), and early Aptian Oceanic Anoxic Event (OAE1a). Modified from the Leg 198 Synthesis (Bralower et al., 2006).

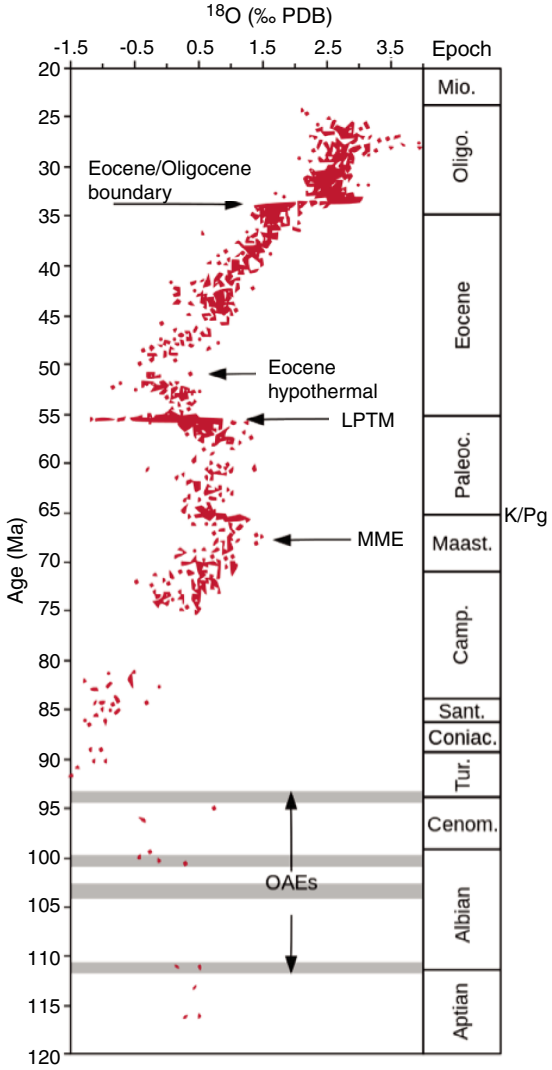

Figure F10. Simulation of ejecta plume from Chicxulub 35 s after impact. Green = basement, gray = projectile and sediments, light blue = atmosphere, dark blue = mantle. Modified from Artemieva and Morgan (2009); from *Icarus*.

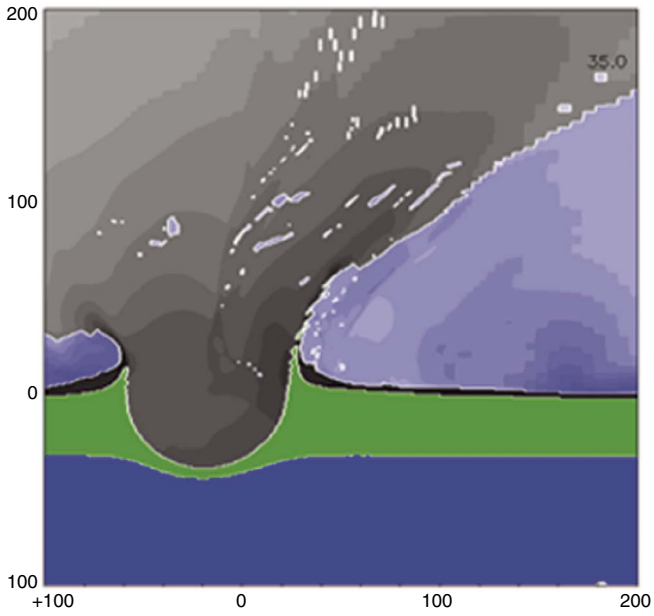

Figure F11. Schematic diagram of Expedition 364 drilling strategy.

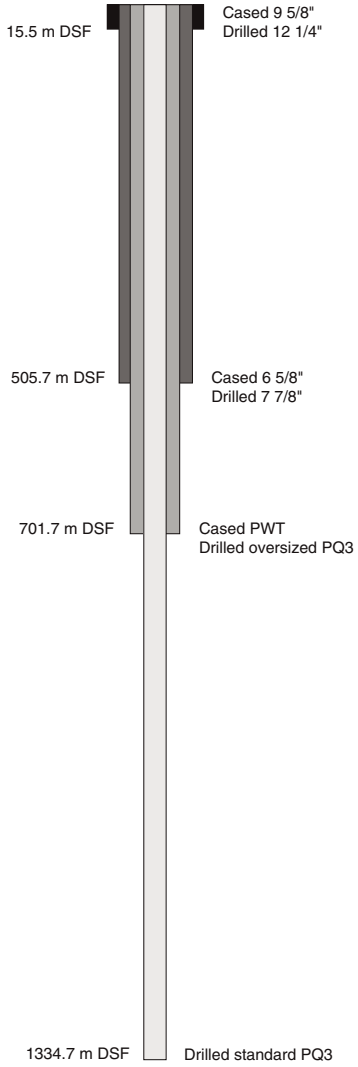

Figure F12. Physical property data, Hole M00077A.

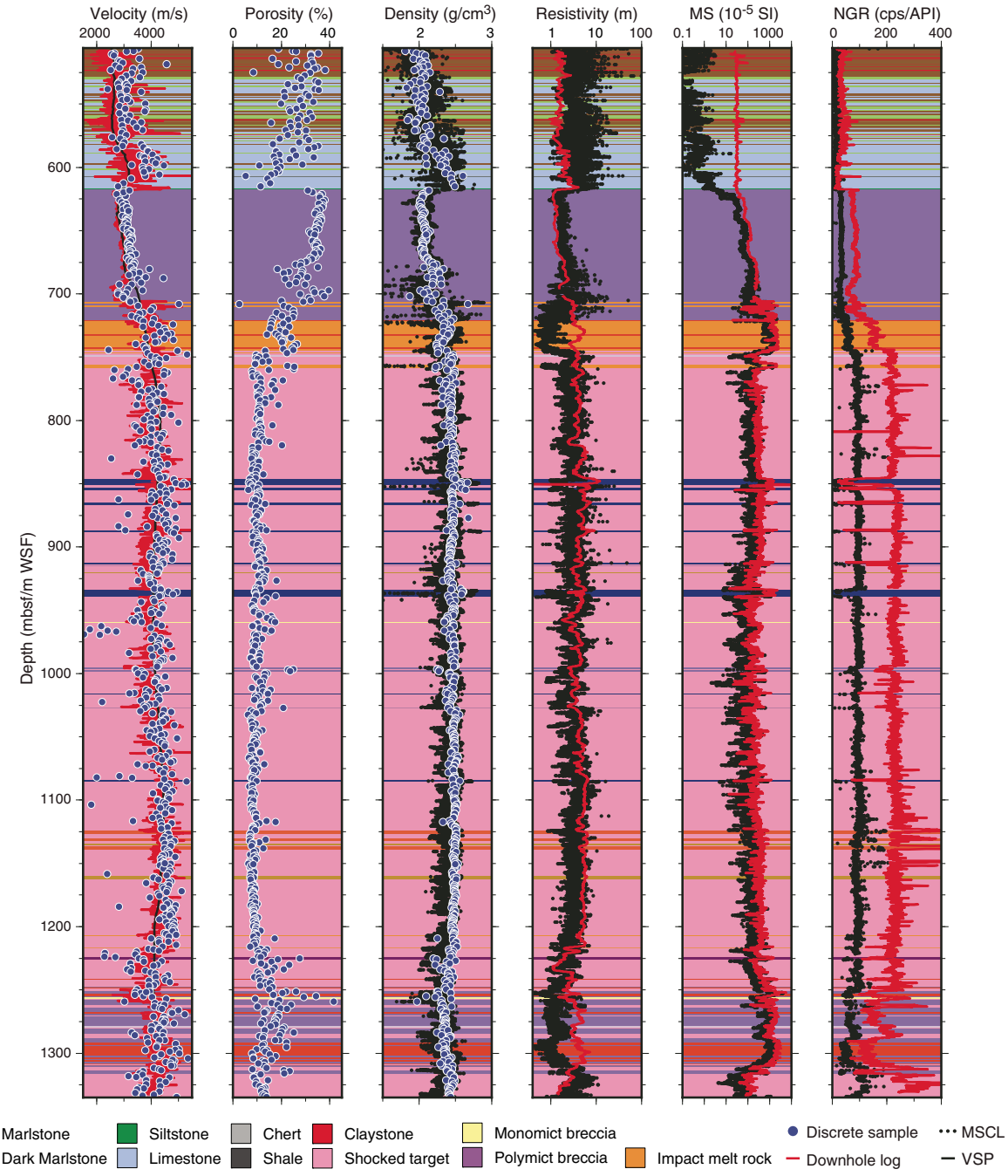

Figure F13. Wireline downhole log data, Hole M0077A. Shallow and deep reading resistivity (RLLS and RLLD), resistivity from induction (Res from IL), conductivity (IL), P-wave sonic (V_P), magnetic susceptibility (MSUS), total gamma ray (GR), borehole fluid temperature (°T TFC), conductivity (Cond FTC), pH and redox, gravity and local magnetic field, borehole tilt and azimuth, amplitude and traveltime acoustic images (ABI Amplitude and ABI TT), borehole diameter (CAL and ACCAL), traveltime cross section of the borehole (ABI TT cross section) and optical borehole image (OBI) See Figure **F12** for lithology key.

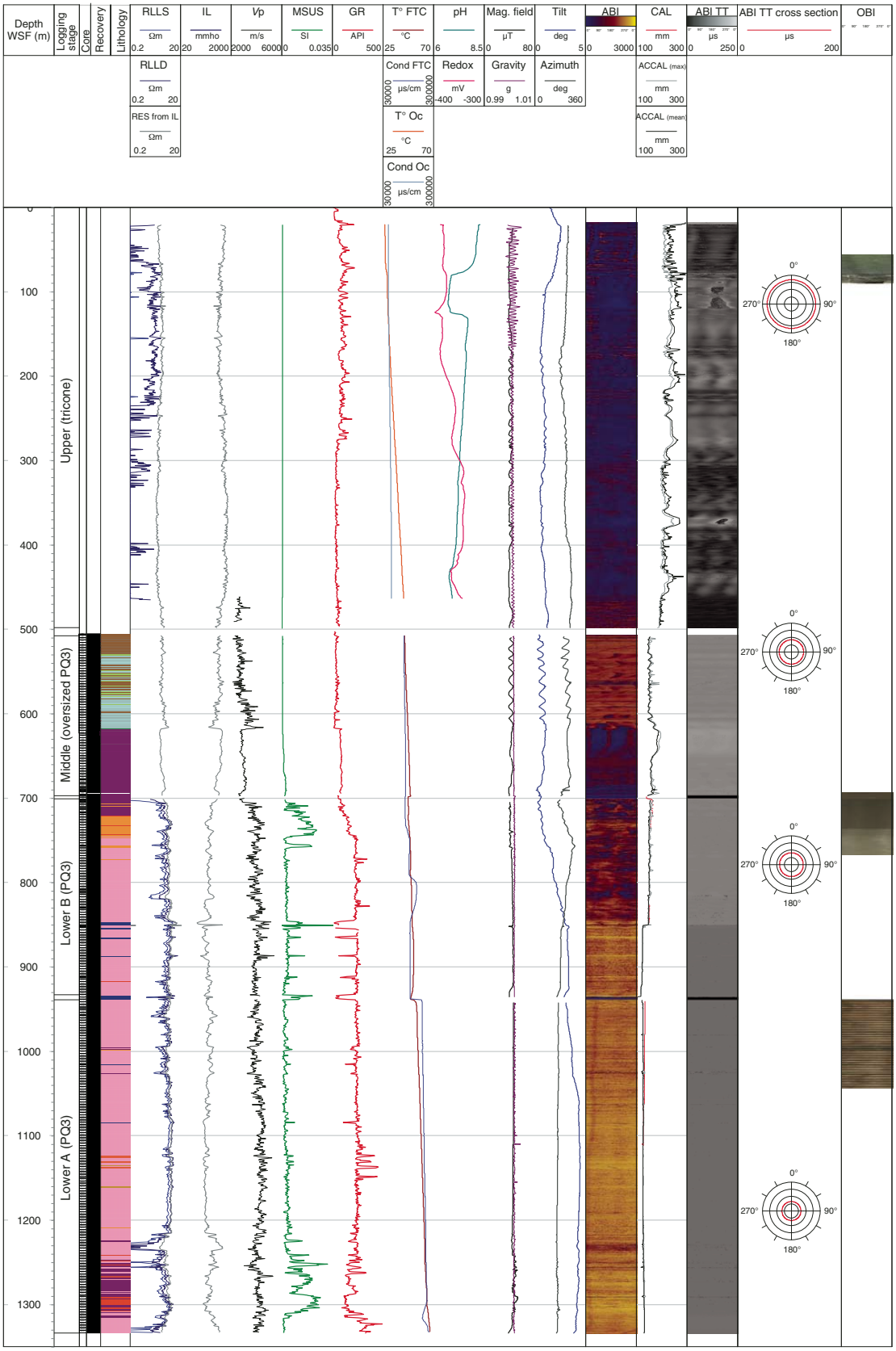

Figure F14. VSP, velocity zones vs. depth regions, and lithostratigraphic units (47.5–1325.0 m WSF), Hole M0077A. Linear best fits are assigned to four manually picked velocity zones (right) and compared to depth regions (left). Lines = upper and lower bounds of *P*-wave velocity using one standard deviation. Lithostratigraphy not available for white regions on right. See Figure **F12** for lithology key.

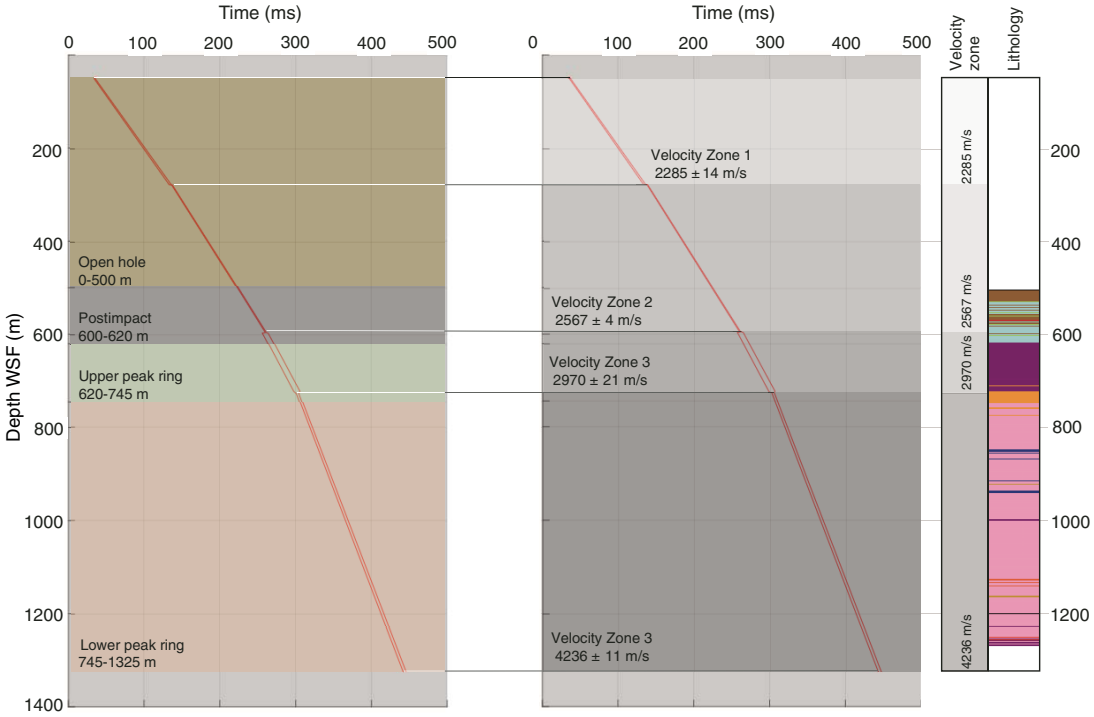

Figure F15. Borehole deviation, Hole M0077A. A. True vertical depth. B. North and east direction of the borehole path.